

Mammographic Feature Enhancement by Multiscale Analysis

Andrew F. Laine, Sergio Schuler, Jian Fan, Walter Huda

Abstract—This paper introduces a novel approach for accomplishing mammographic feature analysis by overcomplete multiresolution representations. We show that efficient representations may be identified within a continuum of scale-space and used to enhance features of importance to mammography. Methods of contrast enhancement are described based on three overcomplete multiscale representations: (1) The dyadic wavelet transform (separable), (2) The φ -transform (non-separable, non-orthogonal), and (3) The hexagonal wavelet transform (non-separable).

Multiscale edges identified within distinct levels of transform space provide local support for image enhancement. Mammograms are reconstructed from wavelet coefficients modified at one or more levels by local and global non-linear operators. In each case, edges and gain parameters are identified adaptively by a measure of energy within each level of scale-space. We show quantitatively that transform coefficients, modified by adaptive non-linear operators, can make more obvious unseen or barely seen features of mammography without requiring additional radiation. Our results are compared with traditional image enhancement techniques by measuring the local contrast of known mammographic features.

We demonstrate that features extracted from multiresolution representations can provide an adaptive mechanism for accomplishing local contrast enhancement. By improving the visualization of breast pathology we can improve chances of early detection while requiring less time to evaluate mammograms for most patients.

Keywords— Wavelet transforms, contrast enhancement, multiscale representations, non-linear operators.

I. INTRODUCTION

Screen/film mammography is widely recognized as being the only effective imaging modality for the early detection of breast cancer in asymptomatic women [1]. Screening asymptomatic women using screen/film mammography has been shown to significantly reduce breast cancer mortality [2]. Breast cancer currently accounts for 32% of cancer incidence and 18% of cancer mortality for women in the United States. There were 182,000 new cases of breast cancer in the United States in 1993 and 46,000 deaths. Five year survival rates are generally very high (93%) for breast cancer staged as being localized, falling to 72% for regional disease and only 18% for distant disease [3]. The early detection of breast cancer is clearly a key ingredient of any strategy designed to reduce breast cancer mortality.

Major advances in screen/film mammography have occurred over the past decade [4] which have resulted in significant improvements in image resolution and film contrast. Of major importance is that these improvements have been achieved at reduced radiation doses. Despite these advances, however, screen/film mammography remains a diagnostic imaging modality where image inter-

pretation remains very difficult. Breast radiographs are generally examined for the presence of malignant masses and indirect signs of malignancy such as the presence of microcalcifications and skin thickening. Unfortunately, it is unlikely that major improvements in imaging performance will be achieved by technical advances in screen/film radiography alone.

The major reason for poor visualization of small malignant masses is the minor difference in x-ray attenuation between normal glandular tissues and malignant disease [5]. This fact makes the detection of small malignancies problematical, especially in younger women who have denser breast tissue. Although calcifications have high inherent attenuation properties, their small size also results in a low subject contrast [6]. As a result, the visibility of small tumors, and any associated microcalcifications, will always be a problem in mammography as it is currently performed using analog film.

Improvements in the ability of screen/film mammography to detect small tumors and microcalcifications is more likely to occur by improving the visibility of these features. It has been suggested that as normally viewed, mammograms display only about 3% of the information they detect! [7].

Our approach to feature analysis and classification is motivated in part by recently discovered biological mechanisms of the human visual system [8]. Both multiorientation and multiresolution are known features of the human visual system. There exist cortical neurons which respond specifically to stimuli within certain orientations and frequencies. In this paper we exploit the orientation and frequency selectivity of wavelet transforms to make mammographic features more obvious through localized contrast gain.

Digital image processing techniques have been applied previously to mammography. The focus of past investigations has been to enhance mammographic features while reducing the enhancement of noise. Gordon and Rangayyan [9] used adaptive neighborhood image processing to enhance the contrast of features relevant to mammography. This method enhanced the contrast of mammographic features as well as noise and digitization effects. Dhawan *et al.* [10], [11], [12] have made significant contributions towards solving problems encountered in mammographic image enhancement. They developed an adaptive neighborhood-based image processing technique that utilized low-level analysis and knowledge about a desired feature in the design of a contrast enhancement function to improve the contrast of specific features. Recently, Tahoces *et al.* [13] developed a method for the enhancement of chest

Andrew F. Laine, Sergio Schuler and Jian Fan are with the Computer & Information Sciences Department, University of Florida, Gainesville, FL 32611.

Walter Huda is with the Department of Radiology, University of Florida, Gainesville, FL 32610.

and breast radiographs by automatic spatial filtering. In their method, they used a linear combination of an original image and two smoothed images obtained from the original image by applying different spatial masks. The process was completed by nonlinear contrast stretching. This spatial filtering enhanced edges while minimally amplifying noise.

Brzakovic *et. al* [14] developed an automated system for the detection and classification of particular types of tumors in digitized mammograms. Their system identified regions corresponding to possible tumors by multiscale image processing based on fuzzy pyramid linking. Regions were subjected to classification by means of deterministic or Bayes classifiers and several metrics. They concluded that their system was very useful in detecting regions that need further analysis, but was less reliable in recognition.

Chan *et. al* [15], [16] investigated the application of computer-based methods for the detection of microcalcifications in digital mammograms. Their system was based on a difference-image technique in which a signal-suppressed image was subtracted from a signal-enhanced image to remove the background in a mammogram. Signal-extraction techniques adapted to the known physical characteristics of microcalcifications were used to isolate them from the remaining noise background. They found that their method could achieve a true-positive cluster detection rate of approximately 80% at a false-positive detection rate of one cluster per image.

Methods of feature enhancement have been key to the success of classification algorithms. Lai *et al.* [17] compared several image enhancement methods for detecting circumscribed masses in mammograms. They compared an edge-preserving smoothing function [18], a half-neighborhood method [19], k-nearest neighborhood, directional smoothing [20] and median filtering [21], and in addition proposed a method of selective median filtering. Among the five techniques implemented, they concluded that selective median filtering with a 5×5 mask performed best for image enhancement and noise removal.

In the fields of image processing and computer vision, transforms such as the windowed Fourier transforms that decompose a signal onto a set of frequency intervals of constant size have been used in many applications, including image compression and texture analysis [22]. Because the spatial and frequency resolutions of these transforms are constant, the information provided by such decompositions is not localized in the spatial domain. A wavelet transform [23], [24], [25], [26], [27], [28] is a decomposition of an image onto a family of functions called a *wavelet family*. In comparison to a windowed Fourier transform which has a fixed resolution in the spatial and frequency domain, the resolution of a wavelet transform varies with a scale parameter, decomposing an image into a set of frequency channels of constant bandwidth on a logarithmic scale. This variation of resolution enables a wavelet transform to “zoom” into the irregularities of an image and characterize them locally.

In this paper we accomplish adaptive contrast enhancement [29], [30], [31] through separable and non-separable multiscale representations. Thus, we decompose an image

into a multiresolution hierarchy of localized information at different spatial frequencies. Our approach for mammographic feature enhancement consists of the application of local and global non-linear operators within levels of a redundant multiresolution representation. We shall present results that suggest our method can emphasize significant features in mammography and improve the visualization of breast pathology.

II. FRAMEWORK FOR MULTISCALE ANALYSIS

In this paper we accomplish mammographic feature analysis through three multiresolution representations: the dyadic wavelet transform [25], the φ -transform or Frazier-Jawerth transform (FJT) [32], and the hexagonal wavelet transform [33]. The representations used in our study are more attractive than traditional multiresolution techniques because perfect reconstruction is possible.

Multiscale wavelet representations suggest a mathematically coherent basis not only for existing multi-grid techniques, but also for exploiting non-linear systems. Multiresolution wavelet analysis provides a natural hierarchy in which to embed an interactive paradigm for accomplishing scale-space feature analysis. Similar to traditional, coarse-to-fine matching strategies, the radiologist may first choose to look for coarse features (e.g. dominant masses) within low-frequency levels of the wavelet transform and later examine finer features (e.g. microcalcifications) at higher frequency levels. Choosing wavelets (or analyzing functions) that are simultaneously localized in both space and frequency results in a powerful methodology for image analysis. The inner-product of a signal f with a wavelet ψ ($\langle f, \psi \rangle = (2\pi)^{-1} \langle \hat{f}, \hat{\psi} \rangle$) reflects the character of f within the time-frequency region where ψ is localized ($\hat{\psi}$ and \hat{f} are the Fourier transforms of the analyzing function and the signal, respectively). If ψ is spatially localized, then two-dimensional features such as shape and orientation are preserved in the transform space and may characterize a feature through scale-space. We may “extract” such features by applying geometric constraints within each level of the transform. We can reduce the complexity of a reconstructed mammogram by selecting only a subset of features that satisfy certain geometric constraints. We may choose to focus on only those features oriented in a particular direction. Subsequent image reconstructions may use the context provided by previously enhanced features to examine (diagnose) additional features emergent at other scales and orientations. For example, fine vertical features may be selected and analyzed in the context of previously classified large horizontal features. Thus, our strategy provides a global context upon which subtle features within finer scales may be classified incrementally through a pre-computed hierarchy of scale-space.

Below, we present a concise overview of the multiresolution representations used in our study, and introduce a notation for the techniques discussed in later sections. In the next section we address the use of non-linear techniques for image enhancement within the context of multiresolu-

tion representations.

A multiresolution representation divides the frequency spectrum of an image x into a low-pass sub-band image y_0^L and a set of band-pass sub-band images y_j^i , $i = 1, \dots, L$, $j = 1, \dots, M$, where L and M denote the number of levels and orientations for a representation, respectively. Notice that a sub-band image without orientation selectivity is denoted by $j = 0$. For example, in the case of an isotropic multiresolution decomposition, $j = 0$ for all levels of the representation. In general, multiresolution representations are implemented by a cascade of analysis/synthesis (A/S) filter banks. For example, Figure 20 shows the implementation of a two-level ($L = 2$) multiresolution representation which partitions orientations into three bands ($M = 3$) by using a cascade of two 4-channel A/S filter banks. The analysis filters, denoted by F , are used to compute the multiresolution decomposition of an image x , while the synthesis filters, denoted by G , are used to reconstruct the original image from its multiresolution representation (transform coefficients). Both, analysis and synthesis sections of the A/S filter bank form a band-splitting system consisting of one low-pass filter, denoted by F_0 and G_0 , respectively, and M band-pass filters, denoted by F_i and G_i , $i = 1, \dots, M$, respectively. Notice that the A/S filter banks are cascaded hierarchically through the low-pass band of the filter bank in order to accomplish a multiresolution representation.

Fig. 1. A two-level 4-channel analysis/synthesis filter bank, where $\Omega = [\omega_x, \omega_y]^T$, \mathbf{K} is the subsampling matrix, and the arrow operators \uparrow and \downarrow denote up-sampling and down-sampling, respectively.

Let F_j^i and G_j^i denote the equivalent filters for the i^{th} level and j^{th} channel of a cascade of analysis and synthesis filters, respectively. Let $W_{ij}[x]$ denote the operation of filtering x with the equivalent filter F_j^i . Then, the sub-band images of an L -level multiresolution decomposition are given by

$$y_j^i = W_{ij}[x]. \tag{1}$$

Similarly, let $W_{ij}^{-1}[y]$ denote the operation of filtering image y with the equivalent filter G_j^i . Then, an L -level multiresolution reconstruction may be written as

$$x = W_{L0}^{-1}[y_0^L] + \sum_{i=1}^L \sum_{j=1}^M W_{ij}^{-1}[y_j^i]. \tag{2}$$

By combining equations (1) and (2) we obtain the general expression for an L -level multiresolution decomposition and reconstruction

$$x = W_{L0}^{-1}[W_{L0}[x]] + \sum_{i=1}^L \sum_{j=1}^M W_{ij}^{-1}[W_{ij}[x]]. \tag{3}$$

The three multiscale transforms used in our study shall follow the general formulation presented above, but are characterized by distinct analysis/synthesis filter banks. In the following subsections, we provide a brief overview of the mathematical formulation for each of the filter banks used

in our investigation. For consistency and clarity, we adopt the above notation throughout the paper.

A. Dyadic Wavelet Transform

Mallat and Zhong [25] showed that a two-dimensional dyadic wavelet transform can be easily constructed from one-dimensional wavelets. Two-dimensional analysis filters implementing a dyadic wavelet transform may be derived from one dimensional dimensional dyadic filters H , G and K as follows

$$\begin{aligned} F_0(\omega_x, \omega_y) &= H(\omega_x)H(\omega_y), \\ F_1(\omega_x, \omega_y) &= G(\omega_x), \\ F_2(\omega_x, \omega_y) &= G(\omega_y), \end{aligned}$$

where H , G and K satisfy $|H(\omega)|^2 + G(\omega)K(\omega) = 1$.

Synthesis filters are easily obtained by

$$\begin{aligned} G_0(\omega_x, \omega_y) &= H^*(\omega_x)H^*(\omega_y), \\ G_1(\omega_x, \omega_y) &= K(\omega_x)L(\omega_y), \\ G_2(\omega_x, \omega_y) &= L(\omega_x)K(\omega_y), \end{aligned}$$

where $L(\omega)$ is the transfer function of a one-dimensional discrete filter satisfying

$$L(\omega) = \frac{1 + |H(\omega)|^2}{2}.$$

Hence, a two-dimensional dyadic wavelet transform results in a multiresolution representation which partitions orientations into two bands ($M = 2$). Figure 21 displays the magnitude of the set of dyadic filters F_j^i used in our investigation and clearly shows that for the dyadic wavelet transform, orientations are partitioned into horizontal and vertical bands.

Fig. 2. Analyzing filters F_j^i for the dyadic wavelet transform.

In the next subsections we describe two non-separable multiscale representations useful for improving local contrast in mammography.

B. φ -Transform

Laine *et al.* [34] showed that a two-dimensional φ -transform may be implemented by an analysis/synthesis filter bank constructed from isotropic filters ($M = 0$). In this case, the general expression for an L -level multiresolution decomposition and reconstruction is simply reduced to

$$x = \sum_{i=1}^L W_i^{-1}[W_i[x]],$$

where the subindex j has been suppressed for clarity.

In our investigation we use a simple filter design introduced by Laine *et al.* [34] to compute two-dimensional φ -transforms for character recognition applications. In this

case, the set of equivalent analysis filters for an L -level φ -transform is given by

$$F^i(\omega_x, \omega_y) = \begin{cases} \sqrt{\frac{1}{2} \left[1 - \cos \left(\pi \log_2 \left(\frac{2^{i-2}\omega_r}{\pi} \right) \right) \right]}, & \text{for } \frac{\pi}{2^i} \leq \omega_r \leq \frac{\pi}{2^{i-2}}, \\ 0, & \text{otherwise,} \end{cases}$$

for $2 \leq i \leq L-1$ and $\omega_r = \sqrt{\omega_x^2 + \omega_y^2}$. For $i=1$ and $i=L$ we have

$$F^1(\omega_x, \omega_y) = \begin{cases} \sqrt{1 - (F^2(\omega_x, \omega_y))^2}, & \text{for } \frac{\pi}{2} \leq \omega_r, |\omega_x| \leq \pi, |\omega_y| \leq \pi \\ 0, & \text{otherwise,} \end{cases}$$

and

$$F^L(\omega_x, \omega_y) = \begin{cases} \sqrt{1 - (F^{L-1}(\omega_x, \omega_y))^2}, & \text{for } 0 \leq \omega_r \leq \frac{\pi}{2^{L-2}}, \\ 0, & \text{otherwise,} \end{cases}$$

respectively. Equivalent synthesis filters are easily obtained by computing

$$G^i(\omega_x, \omega_y) = F^i(\omega_x, \omega_y), \quad i = 1, \dots, L.$$

Figure 22 shows the magnitude of the equivalent filters F^i for levels 1 through 6.

Fig. 3. Analyzing filters F^i for the φ -transform.

C. Hexagonal Wavelet Transform

Adelson *et al.* [35] showed that it is possible to develop non-separable multiresolution representations based on hexagonally symmetric analysis/synthesis filter banks. Simoncelli and Adelson [33] showed that a solution to the hexagonal analysis/synthesis filter bank is given by

$$\begin{aligned} F_0(\boldsymbol{\Omega}) &= G_0(-\boldsymbol{\Omega}) = H(\boldsymbol{\Omega}) = H(-\boldsymbol{\Omega}), \\ F_1(\boldsymbol{\Omega}) &= G_1(-\boldsymbol{\Omega}) = \exp(j\boldsymbol{\Omega}^T \mathbf{s}_1) H(\boldsymbol{\Omega} - \mathbf{k}_1^h), \\ F_2(\boldsymbol{\Omega}) &= G_2(-\boldsymbol{\Omega}) = \exp(j\boldsymbol{\Omega}^T \mathbf{s}_2) H(\boldsymbol{\Omega} - \mathbf{k}_2^h), \\ F_3(\boldsymbol{\Omega}) &= G_3(-\boldsymbol{\Omega}) = \exp(j\boldsymbol{\Omega}^T \mathbf{s}_3) H(\boldsymbol{\Omega} - \mathbf{k}_3^h), \end{aligned}$$

where $\boldsymbol{\Omega} = [\omega_x \ \omega_y]^T$ and

$$\mathbf{s}_1 = \begin{bmatrix} 1 \\ 0 \end{bmatrix}, \quad \mathbf{s}_2 = \begin{bmatrix} \frac{1}{2} \\ \frac{\sqrt{3}}{2} \end{bmatrix}, \quad \text{and } \mathbf{s}_3 = \begin{bmatrix} \frac{1}{2} \\ -\frac{\sqrt{3}}{2} \end{bmatrix},$$

for

$$\mathbf{k}_1^h = \begin{bmatrix} \frac{\pi}{\sqrt{3}} \\ \frac{\pi}{\sqrt{3}} \end{bmatrix}, \quad \mathbf{k}_2^h = \begin{bmatrix} 0 \\ \frac{2\pi}{\sqrt{3}} \end{bmatrix}, \quad \text{and } \mathbf{k}_3^h = \begin{bmatrix} \frac{\pi}{\sqrt{3}} \\ -\frac{2\pi}{\sqrt{3}} \end{bmatrix}.$$

A low-pass solution for $H(\boldsymbol{\Omega})$ in the above equations results in a band-splitting system which may be cascaded

hierarchically through the low-pass band of the A/S filter bank to produce a multiresolution representation which partitions orientations into three bands ($M=3$) of 60 degrees. In our study we used hexagonal A/S filter banks with small regions of support for which perfect reconstruction was well approximated [33]. Figure 23 shows the magnitude of the equivalent hexagonal filters F^i for levels 1 and 2.

In the next section, we describe techniques for modifying transform coefficients within *wavelet frames* for contrast enhancement. The first method allows us to emphasize the structure of local features (singularities) within distinct levels of scale-space while the second method is more global in nature.

Fig. 4. Analyzing filters F_j^i for the hexagonal wavelet transform.

III. ENHANCEMENT TECHNIQUES

In this section we describe a general method to accomplish multiscale contrast enhancement. Here, non-linear techniques for image enhancement are applied within the context of multiresolution representations. Below we present a general formula for processing sub-band images to accomplish adaptive contrast enhancement in mammography. Let f be a user-defined function designed to emphasize features of importance within a selected level i . Then, enhanced sub-band images \hat{y}_j^i may be given by

$$\hat{y}_j^i = f(y_j^i). \quad (4)$$

Thus, we obtain an enhanced image \hat{x} from its multiresolution representation by replacing in equation (2) selected sub-band images y_j^i with their enhanced counterparts \hat{y}_j^i . In particular, the image enhancement techniques described below are applied only to band-pass sub-band images of a multiresolution representation. In general, by defining the function f , we can denote specific enhancement schemes for modifying sub-band image coefficients within distinct levels of scale-space.

A. Local Enhancement Techniques

A problem for image enhancement in mammography is the ability to emphasize mammographic features while *reducing* the enhancement of noise. Multiscale representations localize mammographic features. Previously [30], [31], [36], we presented a local enhancement technique for digital mammography based on multiscale edges. In this study, enhanced sub-band images $\hat{y}_j^i = f(y_j^i)$ were given by

$$\hat{y}_j^i(n_1, n_2) = \begin{cases} y_j^i(n_1, n_2), & \text{if } e_j^i(n_1, n_2) \leq T_j^i, \\ g_j^i y_j^i(n_1, n_2), & \text{if } e_j^i(n_1, n_2) > T_j^i, \end{cases}$$

where n_1 and n_2 denote coordinates in the spatial domain, e_j^i is the edge set corresponding to y_j^i , and g_j^i and T_j^i are the local gain and threshold at level i , respectively.

Formal definitions of the edge set for each of the multiscale representations used in this investigation are presented in the next subsections. Multiscale edges e_j^i are used

as an “index” to increase the local gain of sub-band image coefficients and to emphasize significant features “living” within level i of the transform space. We have found that an effective strategy to adaptively select the threshold value is to set T_j^i proportional to the standard deviation of pixel values in each y_j^i , that is

$$T_j^i = \frac{1}{2} \sqrt{\frac{1}{N^2} \sum_{n_1=1}^N \sum_{n_2=1}^N (y_j^i(n_1, n_2) - m_y)^2} \quad (5)$$

where m_y is the mean value of y_j^i and $N \times N$ is the size of the image. Thus for each band-pass image the threshold value is directly related to the energy of the image within that band (wavelet sub-space). Similarly, g_j^i may be bound adaptively by

$$g_j^i = \frac{T_j^{i \max}}{T_j^i},$$

where

$$T_j^{i \max} = \max\{T_j^i, 1 \leq i \leq L\}$$

for $j = 1, \dots, M$.

Notice that by using a global threshold in each sub-band image we assume that the noise level is position independent. In practice, noise characteristics of digitized mammograms depend on the grey level itself and a noise equalization step [37] should be carried out before processing.

In the next section, we describe how e_j^i was obtained for each of the multiscale representations used in our investigation.

A.1 Dyadic Wavelet Multiscale Edges

For the dyadic wavelet transform [25] we compute multiscale edges by detecting the modulus μ^i and angle α^i of sub-band images y_1^i and y_2^i as follows

$$\begin{aligned} \mu^i(n_1, n_2) &= \sqrt{(y_1^i(n_1, n_2))^2 + (y_2^i(n_1, n_2))^2} \\ \alpha^i(n_1, n_2) &= \arctan\left(\frac{y_2^i(n_1, n_2)}{y_1^i(n_1, n_2)}\right), \end{aligned}$$

where $\alpha^i(n_1, n_2)$ is approximated to the closest orientation defined over an eight-pixel neighborhood. At level i we define the dyadic-maxima $m^i(n_1, n_2)$ as

$$m^i(n_1, n_2) = \begin{cases} \mu^i(n_1, n_2), & \text{if } \mu^i(n_1, n_2) \text{ is maximum} \\ & \text{along the gradient} \\ & \text{direction } \alpha^i(n_1, n_2), \\ 0, & \text{otherwise.} \end{cases}$$

Multiscale edges at level i were then obtained by $e_1^i = e_2^i = m^i$. Figure 24 shows the set of images used to identify two-dimensional wavelet-maxima coefficients for the mammogram shown in Figure 25. The photographs shown in the leftmost column were obtained by combining wavelet coefficients oriented along the x and y directions. Thus, a single picture is shown for each distinct level. Note the clear geometric shape of the calcifications seen at the finer

levels of the scale-space and the definition of the fibroglandular patterns throughout the dense tissue. The photographs in the middle column show the orientation of the coefficients at each level. For purpose of display, the range 0 to 360 degrees has been mapped onto the gray scale values 0 to 255. The wavelet-maxima coefficients are shown as binary images in the rightmost column of Figure 24. As mentioned earlier, these representations shall define a local index for an adaptive weight function applied to corresponding wavelet coefficients within each level of transform space.

Fig. 5. (a) Combination of horizontal and vertical components of dyadic wavelet coefficients for levels 1,2 and 3, respectively (top to bottom) for the mammogram in Figure 6(a). (b) Phase of the combined coefficients. (c) Two-dimensional wavelet maxima coefficients shown as binary edges.

Fig. 6. (a) Original dense mammogram, M41. (b) Enhancement by unsharp masking. (c) Local enhancement by multiscale edges of dyadic wavelet transform coefficients.

A.2 φ -Transform Multiscale Edges

For the φ -transform we compute multiscale edges e^i by first detecting the φ -maxima along four distinct directions defined as follows

$$\begin{aligned} m_1^i(n_1, n_2) &= \begin{cases} |y^i(n_1, n_2)|, & \text{if } |y^i(n_1, n_2)| > |y^i(n_1 + 1, n_2)| \text{ and} \\ & |y^i(n_1, n_2)| > |y^i(n_1 - 1, n_2)|, \\ 0, & \text{otherwise,} \end{cases} \\ m_2^i(n_1, n_2) &= \begin{cases} |y^i(n_1, n_2)|, & \text{if } |y^i(n_1, n_2)| > |y^i(n_1 + 1, n_2 + 1)| \\ & \text{and } |y^i(n_1, n_2)| > |y^i(n_1 - 1, n_2 - 1)|, \\ 0, & \text{otherwise,} \end{cases} \\ m_3^i(n_1, n_2) &= \begin{cases} |y^i(n_1, n_2)|, & \text{if } |y^i(n_1, n_2)| > |y^i(n_1, n_2 + 1)| \text{ and} \\ & |y^i(n_1, n_2)| > |y^i(n_1, n_2 - 1)|, \\ 0, & \text{otherwise,} \end{cases} \\ m_4^i(n_1, n_2) &= \begin{cases} |y^i(n_1, n_2)|, & \text{if } |y^i(n_1, n_2)| > |y^i(n_1 + 1, n_2 - 1)| \\ & \text{and } |y^i(n_1, n_2)| > |y^i(n_1 - 1, n_2 + 1)|, \\ 0, & \text{otherwise.} \end{cases} \end{aligned}$$

Multiscale edges at level i are then obtained by combining the φ -maxima of the distinct orientations at each level of the transform by

$$e^i = m_1^i + m_2^i + m_3^i + m_4^i.$$

Figure 26 shows the combined φ -maxima edges (adaptively thresholded) at level 4 for the original mammogram shown in Figure 27.

Fig. 7. Example of combined orientations of φ edges obtained from level 4 coefficients for the mammogram shown in Figure 8(a).

Fig. 8. (a) Original dense mammogram, M56. (b) Enhancement by histogram equalization. (c) Global enhancement by multiscale histogram equalization of dyadic wavelet coefficients.

A.3 Hexagonal Wavelet Multiscale Edges

For the hexagonal wavelet transform, sub-band images y_1^i , y_2^i , and y_3^i partition orientations into 60, 0, and -60 degree bands, respectively. Multiscale edges e_1^i , e_2^i , and e_3^i at level i are obtained simply by computing the hexagonal-maxima at 60, 0, and -60 degrees, respectively. Figure 28 shows the union of multiscale edges e_1^i , e_2^i , and e_3^i at level 3 for the mammogram shown in Figure 29.

Fig. 9. Combined orientations of hexagonal edges obtained from level 3 coefficients for the mammogram in Figure 10(b).

Fig. 10. (a) Mathematical phantom. (b) Mammogram M56 blended with phantom shown in (a).

B. Global Enhancement Techniques

In this section we present two global enhancement techniques designed in our investigation: multiscale histogram equalization and multiscale adaptive gain.

B.1 Multiscale Histogram Equalization

Histogram equalization of sub-band images provides a global method to accomplish multiresolution enhancement. We simply define a cumulative density function f as

$$f(y) = \int_{y_{min}}^y \rho_y(w)dw + y_{min},$$

where $\rho_y(w) = p_y(w)(y_{max} - y_{min})$, and $p_y(w)$ is the probability density function of y . Notice that $f(y)$ is a single-valued, monotonically increasing function in the range $[y_{min}, y_{max}]$ and satisfies $f(y_{min}) = y_{min}$, $f(y_{max}) = y_{max}$.

B.2 Multiscale Adaptive Gain

Histogram equalization enhances all pixels uniformly. In a second approach, we suppress pixel values of very small amplitude, and enhance only those pixels that are larger than a certain threshold T within each level of transform space. We have designed the following function to accomplish this non-linear operation:

$$f(y) = a [\text{sigm}(c(y - b)) - \text{sigm}(-c(y + b))], \quad (6)$$

where

$$a = \frac{1}{\text{sigm}(c(1 - b)) - \text{sigm}(-c(1 + b))},$$

$$0 < b < 1,$$

$\text{sigm}(y)$ is defined by

$$\text{sigm}(y) = \frac{1}{1 + e^{-y}},$$

and, b and c control the threshold and rate of enhancement, respectively. It can be easily shown that $f(y)$ is *continuous* and monotonically increasing within the interval $[-1, 1]$ (similar to histogram equalization). Furthermore, a derivative of $f(y)$ of any order exists and is continuous. Therefore, enhancement using $f(y)$ will not introduce any new discontinuities. In addition, $f(y)$ satisfies the conditions $f(0) = 0$ and $f(1) = 1$. Figure 30 shows a plot of $f(y)$ for typical values of b and c obtained in our study. Clearly, there always exists a threshold T such that pixels with absolute values larger than T are enhanced, while pixels with absolute values smaller than T are suppressed. The exact value of T can be obtained by solving the non-linear equation $f(y) - y = 0$. However, for simplicity the threshold is controlled through the parameter b . Similarly, we use the standard deviation of pixel values (Equation 5) to adaptively (automatically) select T . Moreover, we define an enhancement rate for $f(y)$ as follows

$$\left. \frac{df}{dy} \right|_{y=b} = ac \left[0.25 + \frac{e^{2bc}}{[1 + e^{2bc}]^2} \right]$$

$$\approx 0.25 ac \text{ for } bc > 2.$$

Hence, effective contrast enhancement can be controlled through the parameter c alone.

Fig. 11. Adaptive gain: $f(y)$ for $b = 0.25$ and $c = 40$ overlaid with $z = y$.

For an input image y with maximum absolute amplitude y_{max} , we map the image range $[-y_{max}, y_{max}]$ onto the interval $[-1, 1]$. This is accomplished by using y_{max} as a normalizing factor in Equation (6). Thus, $f(y)$ may be written as

$$f(y) = a y_{max} [\text{sigm}(c(y/y_{max} - b)) - \text{sigm}(-c(y/y_{max} + b))].$$

The benefit of the normalization is that a , b , and c can be *set independently* of the dynamic range of the input image (a radiograph of unknown density).

IV. EXPERIMENTAL RESULTS AND DISCUSSION

Preliminary results have shown that the multiscale processing techniques described above can make more obvious unseen or barely seen features of a mammogram without requiring additional radiation. Our study suggests that the analyzing functions presented in this paper can improve the visualization of features of importance to mammography and assist the radiologist in the early detection of breast cancer. In our study, film radiographs of the breast were digitized using a sampling distance of 200 microns, on a Kodak laser film digitizer, with 10-bit quantization (contrast resolution). Each digital image was cropped to a matrix size of 512×512 before processing. Although a higher

resolution (100 microns or smaller) is desirable for mammography in clinical practice (especially for the detection and interpretation of microcalcification clusters) the benefit of non-linear multiscale processing remains clear. Due to the inherent nature of multiresolution analysis we would expect similar results for mammographic films digitized at finer resolutions.

Our first image, Figure 25(a) shows a typical radiograph of the breast (poor contrast). Figure 25(c) shows an enhanced image obtained from localization defined by two-dimensional multiscale edges of a dyadic transform, shown in Figure 24(c). In this case, wavelet coefficients associated with the multiscale edges from level two alone were modified locally by adaptive scale-space weights, as described in Section 3.1.1. Note that the emphasis on details at level two alone improved the local contrast of both micro and macro calcification clusters not visible in the original low-contrast mammogram. For comparison, Figure 25(b) shows the result of enhancement by unsharp masking. Fewer details are revealed in comparison to the multiscale method.

Figure 27(a) shows a “dense” mammogram. This class of mammogram is more typical in younger females due to the greater absorption of X-ray energy by less fatty tissues in the breast. They remain particularly difficult to diagnose due to lack of contrast, even for radiologists specializing in mammography. Figure 27(c) shows the result of global wavelet processing for four levels of analysis. In this case, the values of transform coefficients within each level of a dyadic decomposition (excluding the DC cap) were modified by histogram equalization independently. Since the coefficients are space-frequency representations, contrast modifications on the transform side are preserved in part on the spatial side. Similar contrast gains were observed for additional dense radiographs. Figure 27(b) displays the result of standard histogram equalization. Unfortunately, the dense tissues of the breast image are “washed out” in Figure 27(b).

Figure 31(a) shows a mammogram containing a spicular mass. The lack of sharpness is most probably due to poor screen-film contact. Figure 31(c) shows the result of adaptive multiscale processing using the non-separable, non-orthogonal analyzing function described earlier in Section 2.2. In this example, histogram modification was accomplished for an eight-level decomposition via the method of multiscale adaptive gain. Radiologists have observed that the subtle features including calcifications and the penetration of fibroglandular structures into the obvious mass tissue are made more clear in Figure 31(c). In addition, the geometric shapes of calcifications (important for diagnosis) are made more visible and improved definition is seen in the ductules (intra- and extra-lobular units) as well as in the arterial structures within the less-dense tissue of the breast. Figure 31(b) shows the result of standard adaptive histogram equalization. Unfortunately, large areas of the breast are obscured in Figure 31(b).

Mathematical models of phantoms were constructed to validate our enhancement techniques against false positives

Fig. 12. (a) Mammogram with spicular mass, M73. (b) Enhancement by adaptive histogram equalization. (c) Global enhancement by multiscale adaptive gain processing of φ -transform coefficients.

Fig. 13. Blended mammogram: (a) Enhancement by unsharp masking. (b), (c) and (d) Local enhancement by multiscale edges obtained from the dyadic wavelet transform, φ -transform, and hexagonal wavelet transform coefficients, respectively.

arising from possible artifacts introduced by the analyzing functions and to compare our methods against traditional image processing techniques of improving contrast. Our models included features of regular and irregular shapes and sizes of interest in mammographic imaging, such as microcalcifications, cylindrical and spicular objects, and conventional masses. Techniques for “blending” a normal mammogram with the images of mathematical models were developed. The purpose of these experiments was to test the *performance* of our processing techniques on inputs known “a priori” using mammograms where the objects of interest were deliberately obscured by normal breast tissues. The “imaging” justification for “blending” is readily apparent; a cancer is visible in a mammogram because of its (slightly) higher X-ray attenuation which causes a lower radiation exposure on the film in the appropriate region of a projected image. Figure 29(b) shows an example of a mammogram whereby the mathematical phantom shown in Figure 29(a) has been blended into a clinically-proven, cancer-free mammogram. The image shown was constructed by adding the amplitude of the mathematical phantom image to the cancer free mammogram followed by local smoothing of the combined image.

Figure 32(a) shows the result after processing the blended mammogram with unsharp masking. Figures 32(b) through 32(d) were obtained after reconstructing the blended mammogram from the dyadic wavelet transform, φ -transform, and hexagonal wavelet transform coefficients modified by multiscale edge sets identified automatically by our adaptive selection technique described in Section 3.1.3. For purposes of comparing contrast, the images in Figure 32 were rescaled by the same linear transformation.

Radiologists at Shands Hospital at the University of Florida validated that processing the blended mammogram with our local enhancement techniques introduced no significant artifacts and preserved the shapes of the known mammographic features (calcifications, dominant masses, and spicular lesions) contained in the original mathematical phantom. Figure 33 shows enlarged areas containing each feature in the processed mammogram for each method of contrast enhancement. As in Figure 32, the images in each row of Figure 33 were rescaled by the same linear transformation. Enhancement by multiscale edges provided a significant improvement in local contrast for each feature included in the blended mammogram. A quantitative measure of contrast improvement can be defined by a Contrast Improvement Index (CII),

$$CII = \frac{C_{\text{Processed}}}{C_{\text{Original}}},$$

Fig. 14. Contrast enhancement for features in blended mammogram. Phantom mammographic features from top to bottom: minute microcalcification cluster, microcalcification cluster, spicular lesion, circular (arterial) calcification, and a well-circumscribed mass. (a) Original image. (b) Enhancement by unsharp masking. (c), (d) and (e) Local enhancement by multiscale edges obtained from the dyadic wavelet transform, φ -transform, and hexagonal wavelet transform coefficients, respectively.

Fig. 15. Sample scan lines displaying local enhancement by the method of multiscale edges of a dyadic wavelet transform: (a) minute microcalcification cluster, (b) microcalcification cluster, (c) spicular lesion, (d) circular (arterial) calcification and (e) well-circumscribed mass.

where $C_{\text{Processed}}$ and C_{Original} are the contrasts for a region of interest in the processed and original images, respectively.

In this paper we adopt a version of the optical definition of contrast introduced by Morrow *et al.* [38]. The contrast C of an object is defined by

$$C = \frac{f - b}{f + b},$$

where f is the mean gray-level value of a particular object in the image, called the *foreground*, and b is the mean gray-level value of a surrounding region called the *background*. This definition of contrast has the advantage of being independent of the actual range of gray levels in the image. With the aid of the mathematical phantom we computed local masks to separate the foreground and background regions of each feature included in the blended mammogram. Table I shows the contrast values for the mammographic features shown in Figure 33 while Table II shows the values for CII. Note that enhancement by multiscale edges performed significantly better than unsharp masking and consistently improved the contrast of each feature. Figures 34 through 36 show the improvement of local contrast accomplished by our local enhancement techniques for a sample scan line profile taken from cross sections of each feature. In all cases contrast was improved by local enhancement of edges while preserving the overall shape of each feature profile.

Figure 37(a) shows the result after processing the blended mammogram with adaptive histogram equalization (AHE). Figures 37(b) through 37(d) were obtained after reconstructing the blended mammogram from the dyadic wavelet transform, φ -transform, and hexagonal wavelet transform coefficients modified by multiscale adap-

Fig. 16. Sample scan lines displaying local enhancement by the method of multiscale edges of a φ -transform: (a) minute microcalcification cluster, (b) microcalcification cluster, (c) spicular lesion, (d) circular (arterial) calcification and (e) well-circumscribed mass.

Fig. 17. Sample scan lines displaying local enhancement for the method of multiscale edges of a hexagonal wavelet transform: (a) minute microcalcification cluster, (b) microcalcification cluster, (c) spicular lesion, (d) circular (arterial) calcification and (e) well-circumscribed mass.

TABLE I

COMPARISON OF CONTRAST VALUES OBTAINED BY UNSHARP MASKING (UNS) AND LOCAL ENHANCEMENT THROUGH MULTISCALE EDGES EXTRACTED FROM DYADIC WAVELET (DYA), φ -TRANSFORM (PHI), AND HEXAGONAL WAVELET (HEX) COEFFICIENTS. MAMMOGRAPHIC FEATURES: MINUTE MICROCALCIFICATION CLUSTER (MMC), MICROCALCIFICATION CLUSTER (MC), SPICULAR LESION (SL), CIRCULAR (ARTERIAL) CALCIFICATION (CC), AND WELL-CIRCUMSCRIBED MASS (WCM).

Contrast values for local enhancement techniques					
Feature	Original	UNS	DYA	PHI	HEX
MMC	0.050	0.091	0.149	0.193	0.139
MC	0.033	0.048	0.147	0.102	0.145
SL	0.024	0.038	0.085	0.077	0.085
CC	0.037	0.060	0.138	0.125	0.110
WCM	0.012	0.012	0.023	0.016	0.026

TABLE II

CII FOR ENHANCEMENT BY UNSHARP MASKING (UNS) AND LOCAL ENHANCEMENT BY MULTISCALE EDGES OBTAINED FROM DYADIC WAVELET (DYA), φ -TRANSFORM (PHI), AND HEXAGONAL WAVELET (HEX) COEFFICIENTS. MAMMOGRAPHIC FEATURES: MINUTE MICROCALCIFICATION CLUSTER (MMC), MICROCALCIFICATION CLUSTER (MC), SPICULAR LESION (SL), CIRCULAR (ARTERIAL) CALCIFICATION (CC), AND WELL-CIRCUMSCRIBED MASS (WCM).

Contrast Improvement Index (CII) for local enhancement techniques				
Feature	UNS	DYA	PHI	HEX
MMC	1.805	2.951	3.823	2.773
MC	1.463	4.499	3.123	4.445
SL	1.565	3.531	3.186	3.548
CC	1.613	3.693	3.353	2.992
WCM	1.051	1.950	1.386	2.349

tive gain processing. Figure 38 shows enlarged areas containing each feature in the processed mammogram for each method of contrast enhancement. For comparison of contrast, images within Figures 37 and 38 were rescaled collectively as in Figures 32 and 33, respectively. Tables III and IV show the contrast values and CII of the mammographic features displayed in Figure 38. Note that adaptive gain processing provided the maximum CII value for the minute microcalcification cluster, while standard histogram equalization and adaptive histogram equalization significantly decreased the contrast of this feature, possibly introducing diagnostic errors (false negatives). Although adaptive histogram equalization provided the maximum CII value for the well-defined mass, it is clear from Figure 38 that multiscale adaptive gain processing better preserved the morphology of the mass and its surrounding structures.

TABLE III

COMPARISON OF CONTRAST VALUES OBTAINED BY STANDARD HISTOGRAM EQUALIZATION (HEQ), ADAPTIVE HISTOGRAM EQUALIZATION (AHE) AND MULTISCALE ADAPTIVE GAIN PROCESSING OF DYADIC WAVELET (DYA), φ -TRANSFORM (PHI), AND HEXAGONAL WAVELET (HEX) COEFFICIENTS. MAMMOGRAPHIC FEATURES: MINUTE MICROCALCIFICATION CLUSTER (MMC), MICROCALCIFICATION CLUSTER (MC), SPICULAR LESION (SL), CIRCULAR (ARTERIAL) CALCIFICATION (CC), AND WELL-CIRCUMSCRIBED MASS (WCM).

Contrast values for global enhancement techniques					
Feature	HEQ	AHE	DYA	PHI	HEX
MMC	0.048	0.030	0.198	0.199	0.222
MC	0.030	0.102	0.204	0.210	0.192
SL	0.022	0.044	0.165	0.164	0.146
CC	0.039	0.113	0.214	0.211	0.201
WCM	0.012	0.159	0.157	0.150	0.105

TABLE IV

CII FOR ENHANCEMENT BY STANDARD HISTOGRAM EQUALIZATION (HEQ), ADAPTIVE HISTOGRAM EQUALIZATION (AHE), AND MULTISCALE ADAPTIVE GAIN PROCESSING OF DYADIC WAVELET (DYA), φ -TRANSFORM (PHI), AND HEXAGONAL WAVELET (HEX) COEFFICIENTS. MAMMOGRAPHIC FEATURES: MINUTE MICROCALCIFICATION CLUSTER (MMC), MICROCALCIFICATION CLUSTER (MC), SPICULAR LESION (SL), CIRCULAR (ARTERIAL) CALCIFICATION (CC), AND WELL-CIRCUMSCRIBED MASS (WCM).

Contrast Improvement Index (CII) for global enhancement techniques					
Feature	HEQ	AHE	DYA	PHI	HEX
MMC	0.935	0.599	3.929	3.951	4.397
MC	0.904	3.126	6.234	6.421	5.865
SL	0.909	1.816	6.861	6.822	6.056
CC	1.046	3.020	5.730	5.663	5.399
WCM	1.017	13.743	13.576	12.992	9.071

V. SUMMARY

In this study, methods for accomplishing adaptive contrast enhancement by multiscale representations have been investigated. Contrast enhancement was applied to features of specific interest to mammography including masses, spicules and microcalcifications. Multiresolution representations provided an adaptive mechanism for the local emphasis of such features blended into digitized mammograms. In general, improvements in image contrast for multiscale image processing algorithms were superior to those obtained using competitive algorithms of unsharp

Fig. 18. Blended mammogram: (a) Enhancement by adaptive histogram equalization. (b), (c) and (d) Global enhancement by multiscale adaptive gain processing of the dyadic wavelet transform, φ -transform, and hexagonal wavelet transform coefficients, respectively.

Fig. 19. Contrast enhancement for features in blended mammogram. Phantom mammographic features from top to bottom: minute microcalcification cluster, microcalcification cluster, spicular lesion, circular (arterial) calcification, and a well-circumscribed mass. (a) Original image. (b) Enhancement by adaptive histogram equalization. (c), (d) and (e) Global enhancement by multiscale adaptive gain processing of the dyadic wavelet transform, φ -transform, and hexagonal wavelet transform coefficients, respectively.

masking and adaptive histogram equalization. These initial results are encouraging and suggest that wavelet based image processing algorithms could play an important role in improving the imaging performance of digital mammography.

Features blended into the mammograms were “idealized” representations of the types of objects that are of primary interest to mammographers. The resultant mammographic images were appropriate for the purpose of demonstrating improved image contrast made possible by wavelet based image processing algorithms. Furthermore, these images were also useful for comparing multiscale wavelet based algorithms with existing image processing algorithms. The test results obtained in this study, however, cannot be directly extrapolated to clinical mammography. Caution is required because the blended mammographic features were ideal features whereas real masses and microcalcifications are likely to be irregular in shape. In addition, it is also important to investigate the introduction of image artifacts by any image processing scheme which may adversely affect imaging performance by increasing the false positive rate.

Although the results obtained in this study are very encouraging, it is essential that further studies are performed to identify the most promising approaches of multiscale based image processing algorithms. The identification of the most appropriate basis functions for enhancing specific types of mammographic features needs further investigation. The best way of selecting wavelet coefficients for enhancement, and their degree of enhancement, also merit systematic analysis. Ultimately, however, the objective of any image processing is to improve the visibility of clinically significant features in mammograms. Accordingly, the most promising algorithms require evaluation using clinical mammograms. Such tests will be designed to measure the ability of multiscale image processing to significantly improve the sensitivity, specificity and overall accuracy of mammographic interpretation.

ACKNOWLEDGMENTS

This work was sponsored in part by the U.S. Army Medical Research and Development Command, Grant number DAMD17-93-J-3003, and the Whitaker Foundation. The authors wish to thank Doctors Edward Staab, Janice Honeyman, and Barbara Steinbach, of the Department of Radiology, University of Florida, for their support and encouragement. Images were provided by the Center for Engineering and Medical Image Analysis and the H. Lee Moffitt Cancer Center and Research Institute at the University of

South Florida.

REFERENCES

- [1] A.G. Haus and M.J. Yaffe, Eds., *A categorical course in physics. Technical aspects of breast imaging*. Radiological Society of North America, 1993, Presented at the 79th scientific assembly and annual meeting of the RSNA.
- [2] S.A. Feig and R.E. Hendrick, "Risk, benefit and controversy in mammographic screening", in *A categorical course in physics. Technical aspects of breast imaging*, A.G. Haus and M.J. Yaffe, Eds. Radiological Society of North America, 1993, pp. 119-135, Presented at the 79th scientific assembly and annual meeting of the RSNA.
- [3] R.A. Smith, "Epidemiology of breast cancer", in *A categorical course in physics. Technical aspects of breast imaging*, A.G. Haus and M.J. Yaffe, Eds. Radiological Society of North America, 1993, pp. 21-33, Presented at the 79th scientific assembly and annual meeting of the RSNA.
- [4] G.T. Barnes and G.D. Frey, Eds., *Screen film mammography. Imaging considerations and medical physics responsibilities*, Madison, Wisconsin, 1991. Medical Physics Publishing.
- [5] P.C. Johns and M.J. Yaffe, "X-ray characterization of normal and neoplastic breast tissues", *Physics in Medicine and Biology*, vol. 32, no. 6, pp. 675-695, Feb. 1987.
- [6] M.J. Yaffe, R.J. Jennings, R. Fahrig, and T.R. Fewell, "X-ray spectral considerations for mammography", in *A categorical course in physics. Technical aspects of breast imaging*, A.G. Haus and M.J. Yaffe, Eds. Radiological Society of North America, 1993, pp. 63-72, Presented at the 79th scientific assembly and annual meeting of the RSNA.
- [7] I. Brodie and R.A. Gutcheck, "Radiographic information theory and application to mammography", *Medical Physics*, vol. 9, 1982.
- [8] T.N. Wiesel, "Postnatal development of the visual cortex and the influence of environment", *Nature*, vol. 299, no. 5883, pp. 583-591, Oct. 1982.
- [9] R. Gordon and R.M. Rangayyan, "Feature enhancement of film mammograms using fixed and adaptive neighborhoods", *Applied Optics*, vol. 23, no. 4, pp. 560-564, Feb. 1984.
- [10] A.P. Dhawan, G. Buelloni, and R. Gordon, "Enhancement of mammographic feature by optimal adaptive neighborhood image processing", *IEEE Transactions on Medical Imaging*, vol. 5, no. 1, pp. 8-15, Mar. 1986.
- [11] A.P. Dhawan and R. Gordon, "Reply to comments on enhancement of mammographic feature by optimal adaptive neighborhood image processing", *IEEE Transactions on Medical Imaging*, vol. 6, no. 1, pp. 82-83, Mar. 1987.
- [12] A.P. Dhawan and E. Le Royer, "Mammographic feature enhancement by computerized image processing", *Computer Methods and Programs in Biomedicine*, vol. 27, no. 1, pp. 23-35, 1988.
- [13] P.G. Tahoces, J. Correa, M. Souto, C. Gonzalez, L. Gomez, and J.J. Vidal, "Enhancement of chest and breast radiographs by automatic spatial filtering", *IEEE Transaction on Medical Imaging*, vol. 10, no. 3, pp. 330-335, Sept. 1991.
- [14] D. Brzakovic, X.M. Luo, and P. Brzakovic, "An approach to automated detection of tumors in mammograms", *IEEE Transaction on Medical Imaging*, vol. 9, no. 3, pp. 232-241, Sept. 1990.
- [15] H.P. Chan, K. Doi, S. Galhotra, C.J. Vyborny, H. MacMahon, and P.M. Jokich, "Image feature analysis and computer-aided diagnosis in digital radiography. automated detection of microcalcifications in mammography", *Medical Physics*, vol. 14, no. 4, pp. 538-548, July 1987.
- [16] H.P. Chan, K. Doi, C.J. Vyborny, K.L. Lam, and R.A. Schmidt, "Computer-aided detection of microcalcifications in mammograms: Methodology and preliminary clinical study", *Investigative Radiology*, vol. 23, no. 9, pp. 664-671, Sept. 1988.
- [17] S. Lai, X. Li, and W.F. Bischof, "On techniques for detecting circumscribed masses in mammograms", *IEEE Transactions on Medical Imaging*, vol. 8, no. 4, pp. 377-386, Dec. 1989.
- [18] M. Nagao and T. Matsuyama, "Edge preserving smoothing", *Computer Graphics and Image Processing*, vol. 9, no. 4, pp. 394-407, Apr. 1979.
- [19] A. Scheer, F.R.D. Velasco, and A. Rosenfield, "Some new image smoothing techniques", *IEEE Transactions on Systems, Man and Cybernetics*, vol. 10, no. 3, pp. 153-158, 1980.
- [20] L.S. Davis and A. Rosenfield, "Noise cleaning by iterated local averaging", *IEEE Transactions on Systems, Man and Cybernetics*, vol. 8, pp. 705-710, 1978.
- [21] A.C. Bovik, T.S. Huang, and D.C. Munson, Jr., "The effect of median filtering on edge estimation and detection", *IEEE Transactions on Pattern Analysis and Machine Intelligence*, vol. 9, no. 2, pp. 181-194, Mar. 1987.
- [22] A. Laine and J. Fan, "Texture classification by wavelet packet signatures", *IEEE Transactions on Pattern Analysis and Machine Intelligence*, vol. 15, no. 11, pp. 1186-1191, Nov. 1993.
- [23] I. Daubechies, "Orthonormal bases of compactly supported wavelets", *Communications on Pure and Applied Mathematics*, vol. 41, pp. 909-996, 1988.
- [24] I. Daubechies, "The wavelet transform, time-frequency localization and signal analysis", *IEEE Transactions on Information Theory*, vol. 36, no. 5, pp. 961-1005, Sept. 1990.
- [25] S. Mallat and S. Zhong, "Characterization of signals from multiscale edges", *IEEE Transactions on Pattern Analysis and Machine Intelligence*, vol. 14, no. 7, pp. 710-732, July 1992.
- [26] S. Mallat, "A theory for multiresolution signal decomposition: The wavelet representation", *IEEE Transactions on Pattern Analysis and Machine Intelligence*, vol. 11, no. 7, pp. 674-693, July 1989.
- [27] S. Mallat, "Multiresolution approximations and wavelet orthonormal bases of $L^2(\mathbb{R})$ ", *Transactions of the American Mathematical Society*, vol. 315, no. 1, pp. 69-87, Sept. 1989.
- [28] S. Mallat, "Multifrequency channel decompositions of images and wavelet models", *IEEE Transactions on Acoustics, Speech, and Signal Processing*, vol. 37, no. 12, Dec. 1989.
- [29] A. Laine, "Multiscale wavelet representations for mammographic feature analysis", in *Image Enhancement Techniques: Computer Science. National Cancer Institute Breast Imaging Workshop: State-of-the-Art and New Technologies*, Bethesda, Maryland, Sept. 1991.
- [30] A. Laine and S. Song, "Multiscale wavelet representations for mammographic feature analysis", in *Proceedings of SPIE. Conference on Mathematical Methods in Medical Imaging*, San Diego, California, July 1992.
- [31] A. Laine and S. Song, "Wavelet processing techniques for digital mammography", in *Proceedings of SPIE. Conference on Visualization in Biomedical Computing*, Chapel Hill, North Carolina, Oct. 1992.
- [32] M. Frazier, B. Jawerth, and G. Weiss, "Littlewood-paley theory and the study of function spaces", in *Conference board of the mathematical sciences. Regional conference series in mathematics*, 1991, number 79.
- [33] E.P. Simoncelli and E.H. Adelson, "Non-separable extensions of quadrature mirror filters to multiple dimensions", *Proceedings of the IEEE*, vol. 78, no. 4, pp. 652-664, Apr. 1990.
- [34] A. Laine, W. Ball, and A. Kumar, "A multiscale approach for recognizing complex annotations in engineering documents", in *Proceedings 1991 IEEE Computer Society Conference on Computer Vision and Pattern Recognition*, Lahaina, Maui, Hawaii, June 1991.
- [35] E.H. Adelson, E. Simoncelli, and R. Higorani, "Orthogonal pyramid transforms for image coding", in *Proceedings of SPIE*, Oct. 1987.
- [36] A. Laine and S. Schuler, "Hexagonal wavelet processing of digital mammography", in *Medical Imaging 1993*, Newport Beach, California, Feb. 1993, Part of SPIE's Thematic Applied Science and Engineering Series.
- [37] N. Karsseneijer, "Adaptive noise equalization and image analysis in mammography", in *International Conference on Information Processing in Medical Imaging. Lecture Notes in Computer Science 687*, 1993, pp. 472-486.
- [38] W.M. Morrow, R.B. Paranjape, R.M. Rangayyan, and J.E.L. Desautels, "Region-based contrast enhancement of mammograms", *IEEE Transactions on Medical Imaging*, vol. 11, no. 3, pp. 392-406, Sept. 1992.

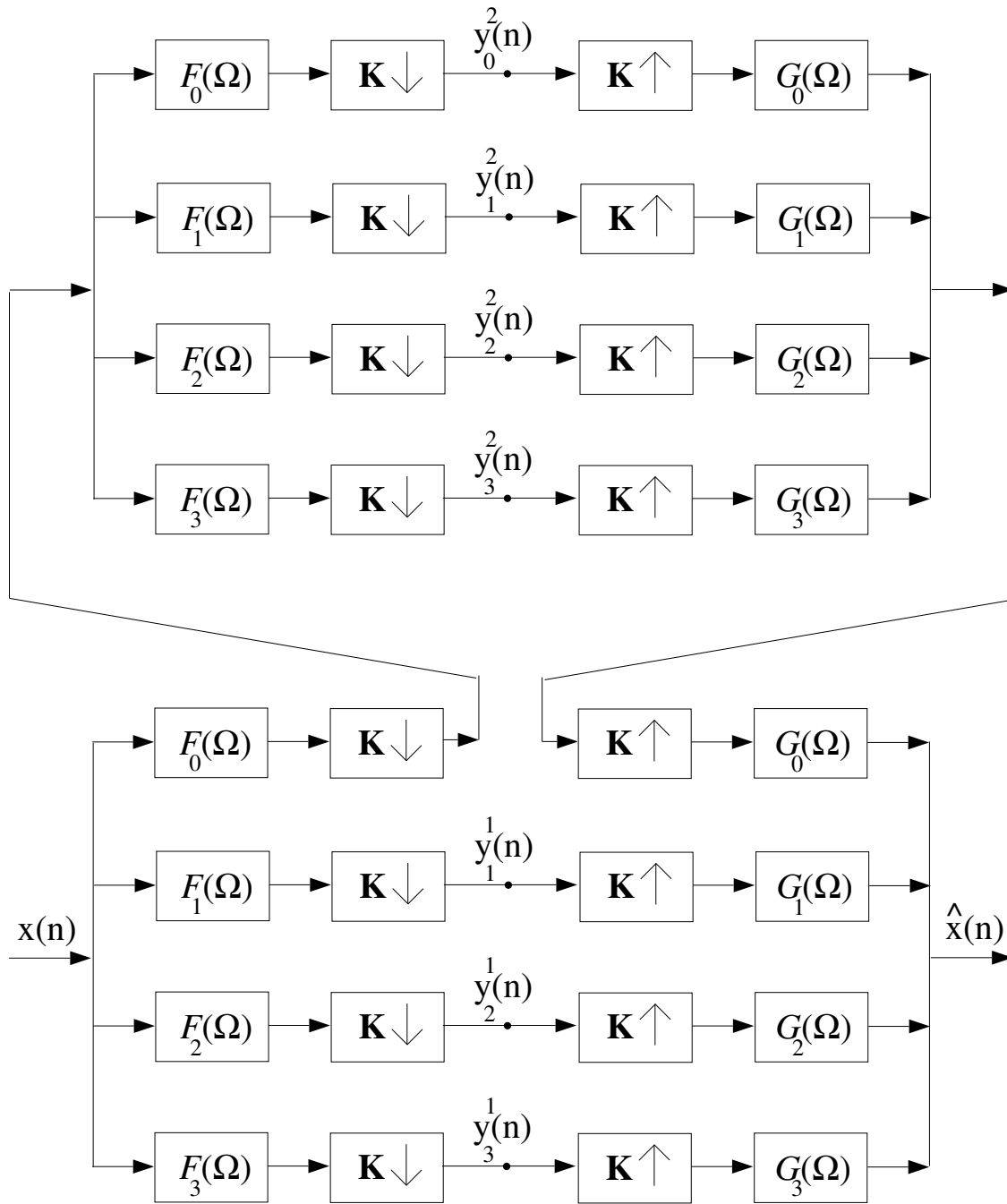


Fig. 1. A two-level 4-channel analysis/synthesis filter bank, where $\Omega = [\omega_x, \omega_y]^T$, \mathbf{K} is the subsampling matrix, and the arrow operators \uparrow and \downarrow denote up-sampling and down-sampling, respectively.

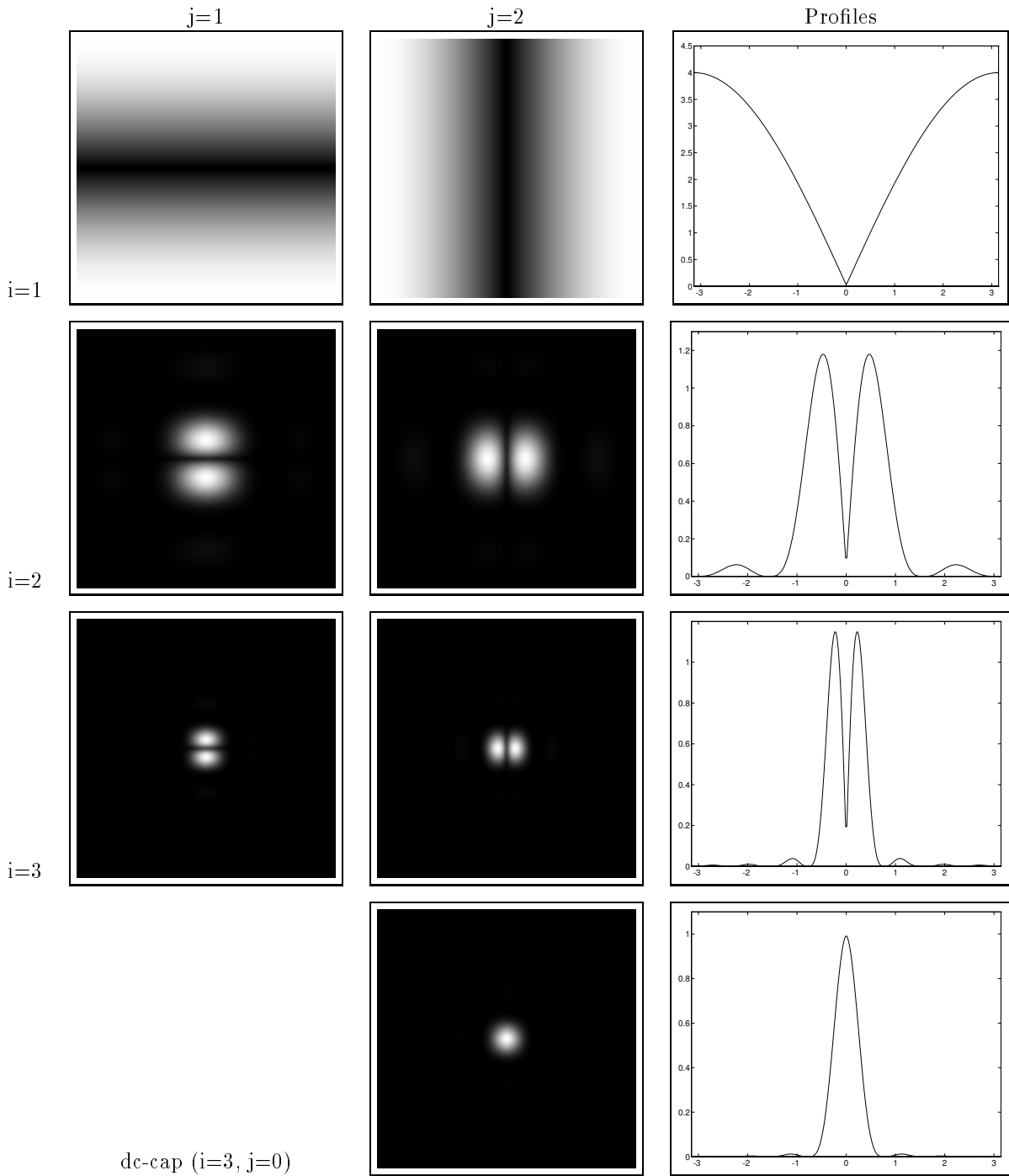


Fig. 2. Analyzing filters F_j^i for the dyadic wavelet transform.

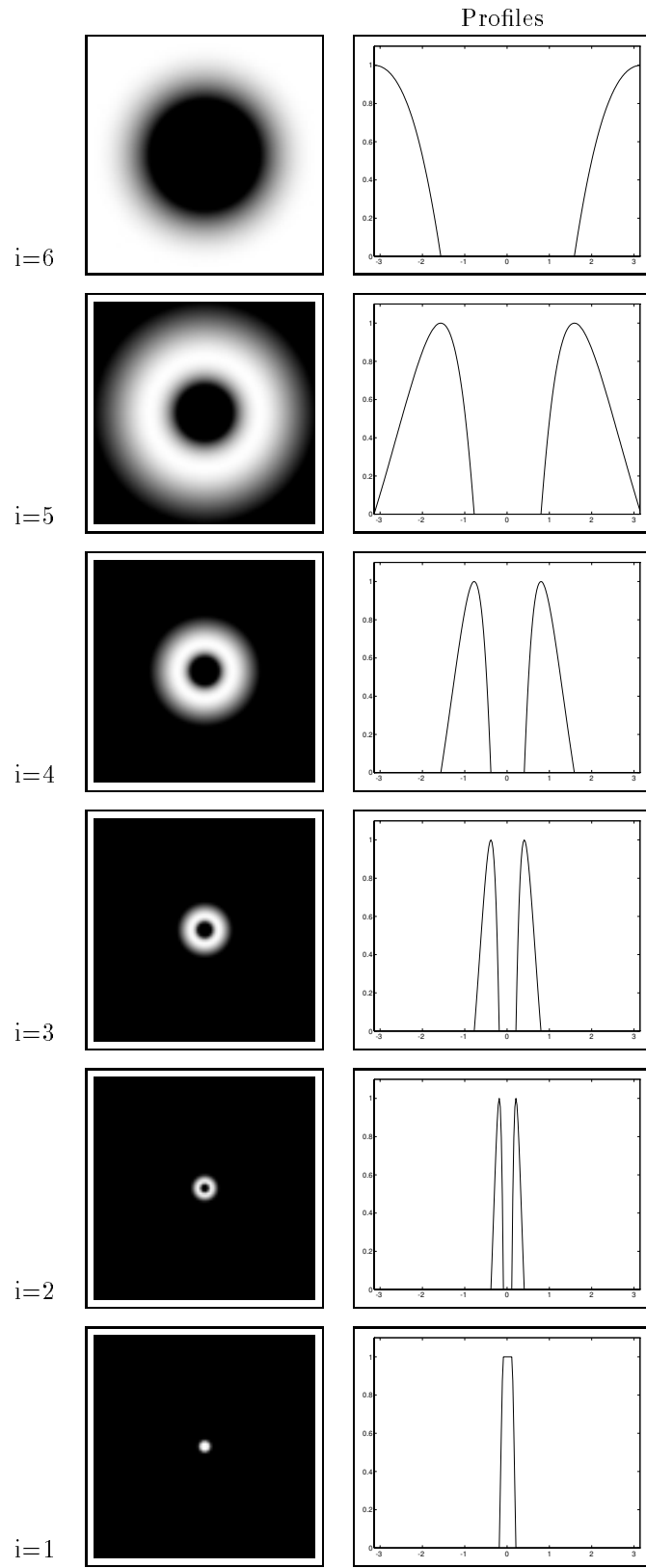


Fig. 3. Analyzing filters F^i for the φ -transform.

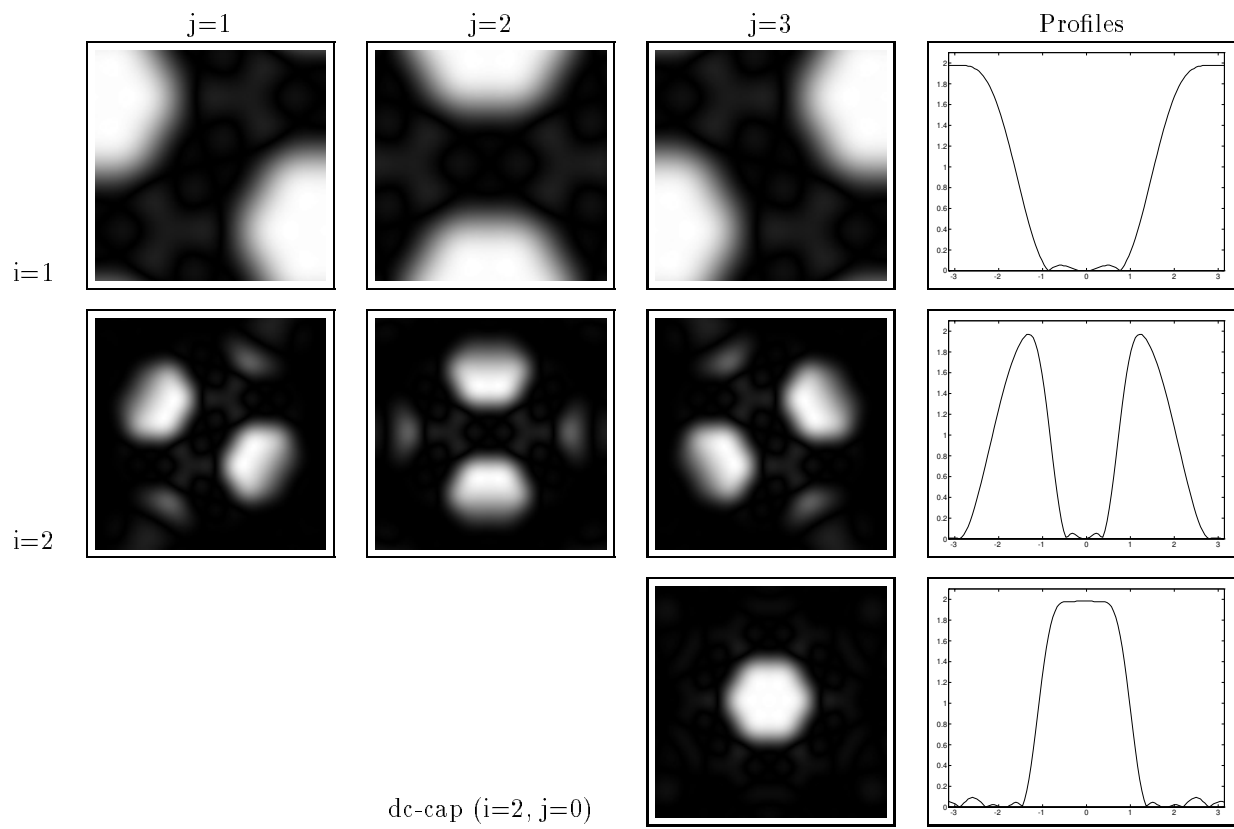


Fig. 4. Analyzing filters F_j^i for the hexagonal wavelet transform.

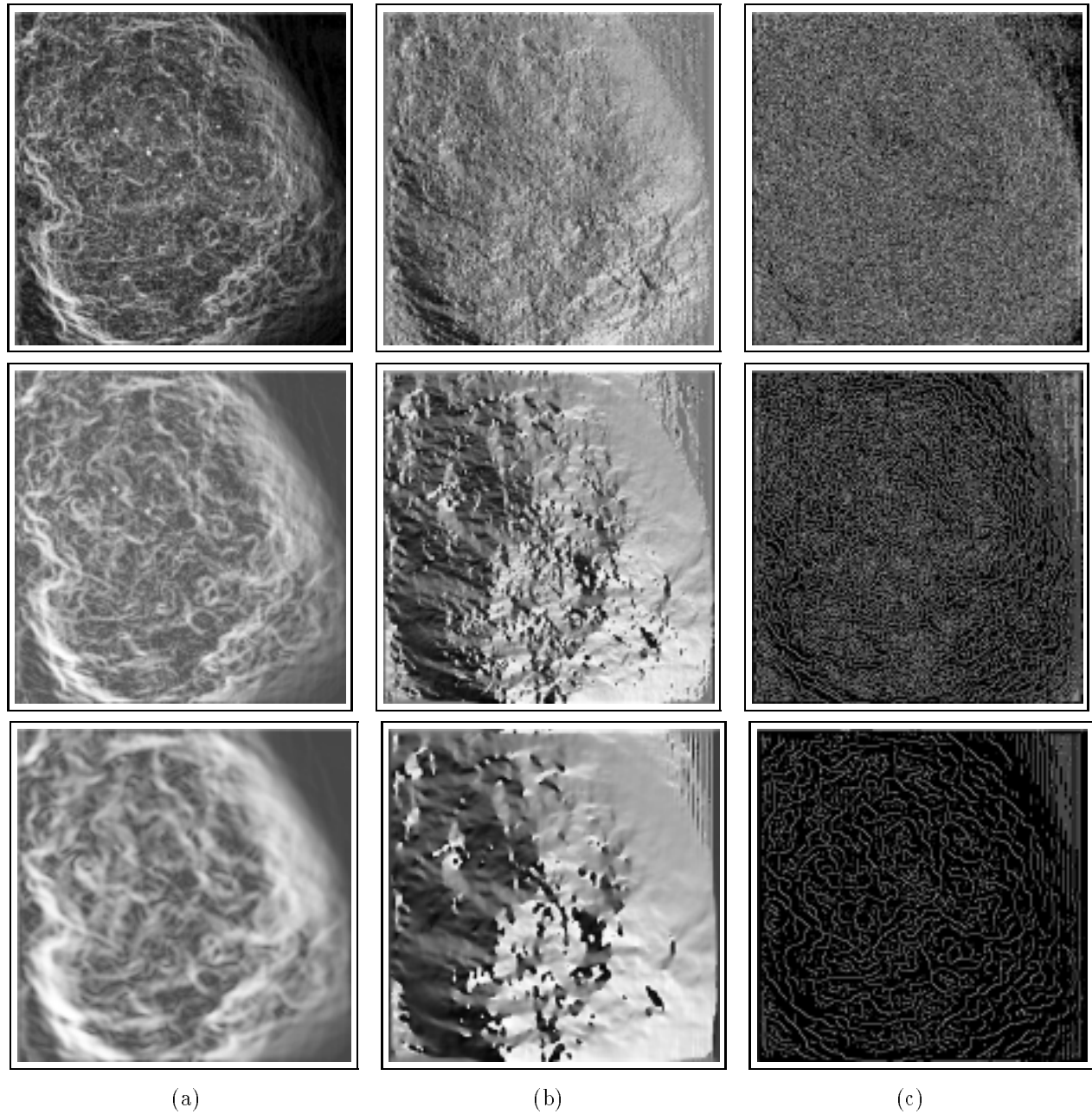


Fig. 5. (a) Combination of horizontal and vertical components of dyadic wavelet coefficients for levels 1,2 and 3, respectively (top to bottom) for the mammogram in Figure 6(a). (b) Phase of the combined coefficients. (c) Two-dimensional wavelet maxima coefficients shown as binary edges.

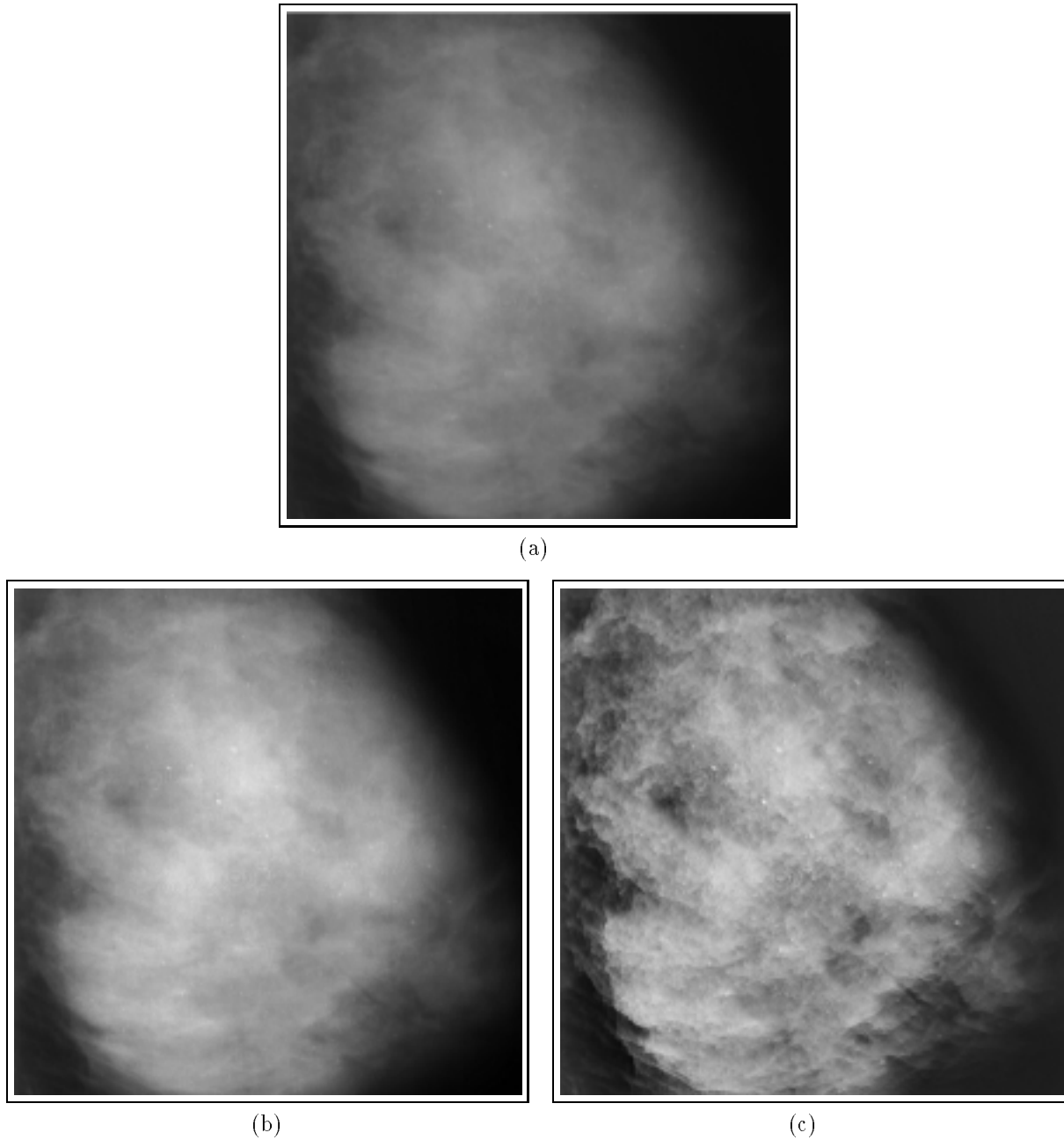


Fig. 6. (a) Original dense mammogram, M41. (b) Enhancement by unsharp masking. (c) Local enhancement by multiscale edges of dyadic wavelet transform coefficients.

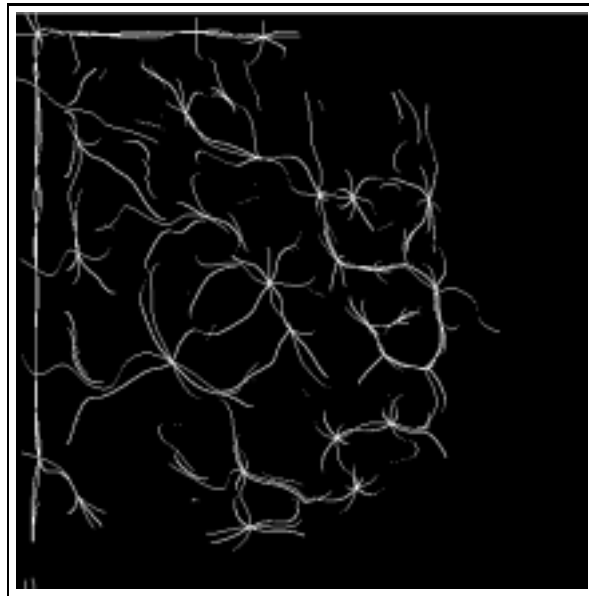
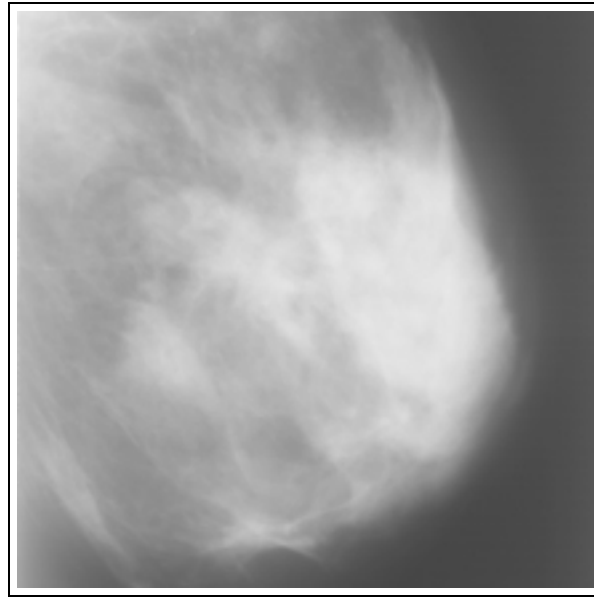
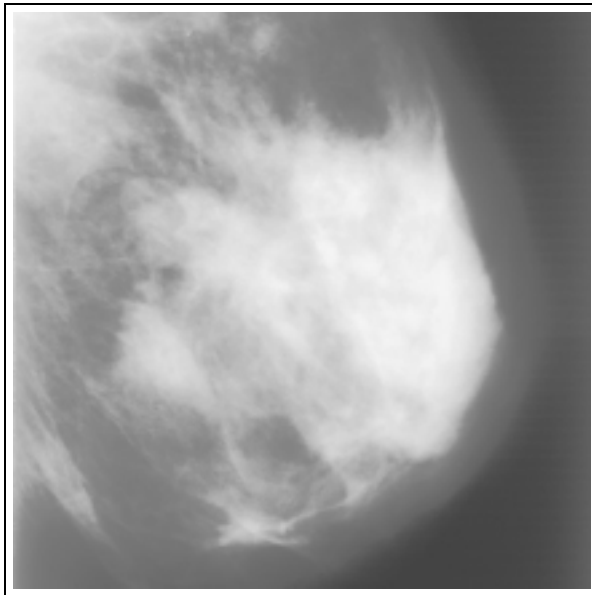


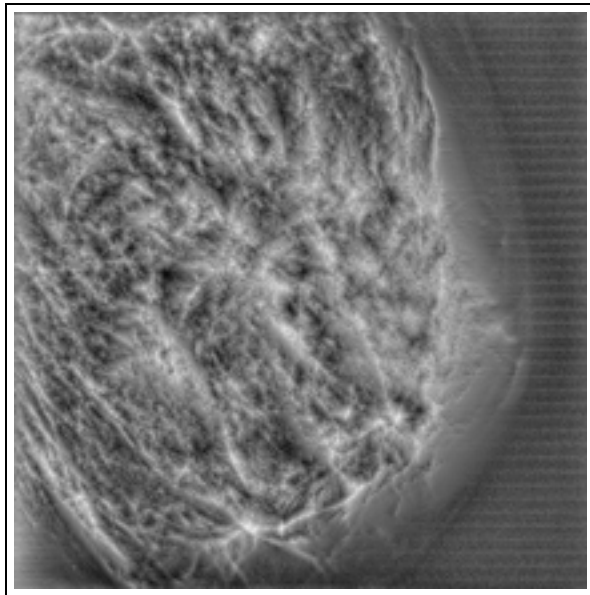
Fig. 7. Example of combined orientations of φ edges obtained from level 4 coefficients for the mammogram shown in Figure 8(a).



(a)



(b)



(c)

Fig. 8. (a) Original dense mammogram, M56. (b) Enhancement by histogram equalization. (c) Global enhancement by multiscale histogram equalization of dyadic wavelet coefficients.

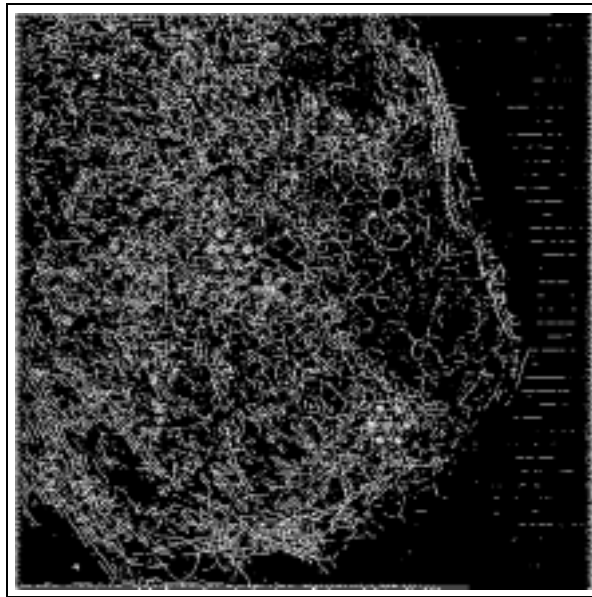


Fig. 9. Combined orientations of hexagonal edges obtained from level 3 coefficients for the mammogram in Figure 10(b).

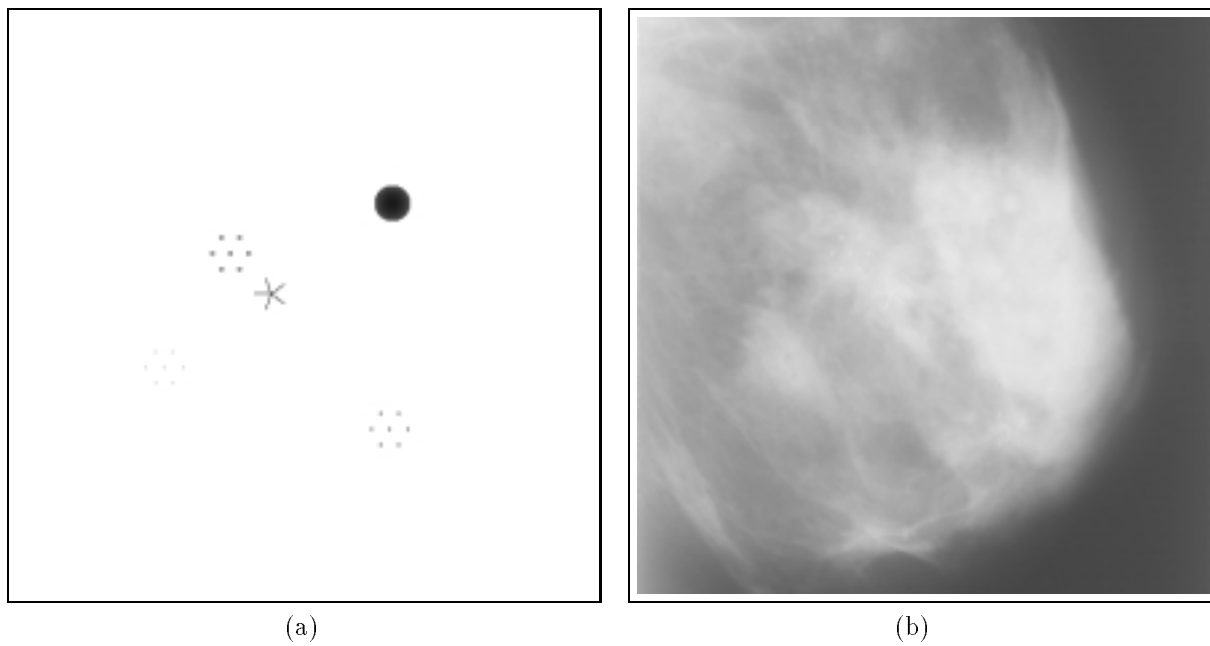


Fig. 10. (a) Mathematical phantom. (b) Mammogram M56 blended with phantom shown in (a).

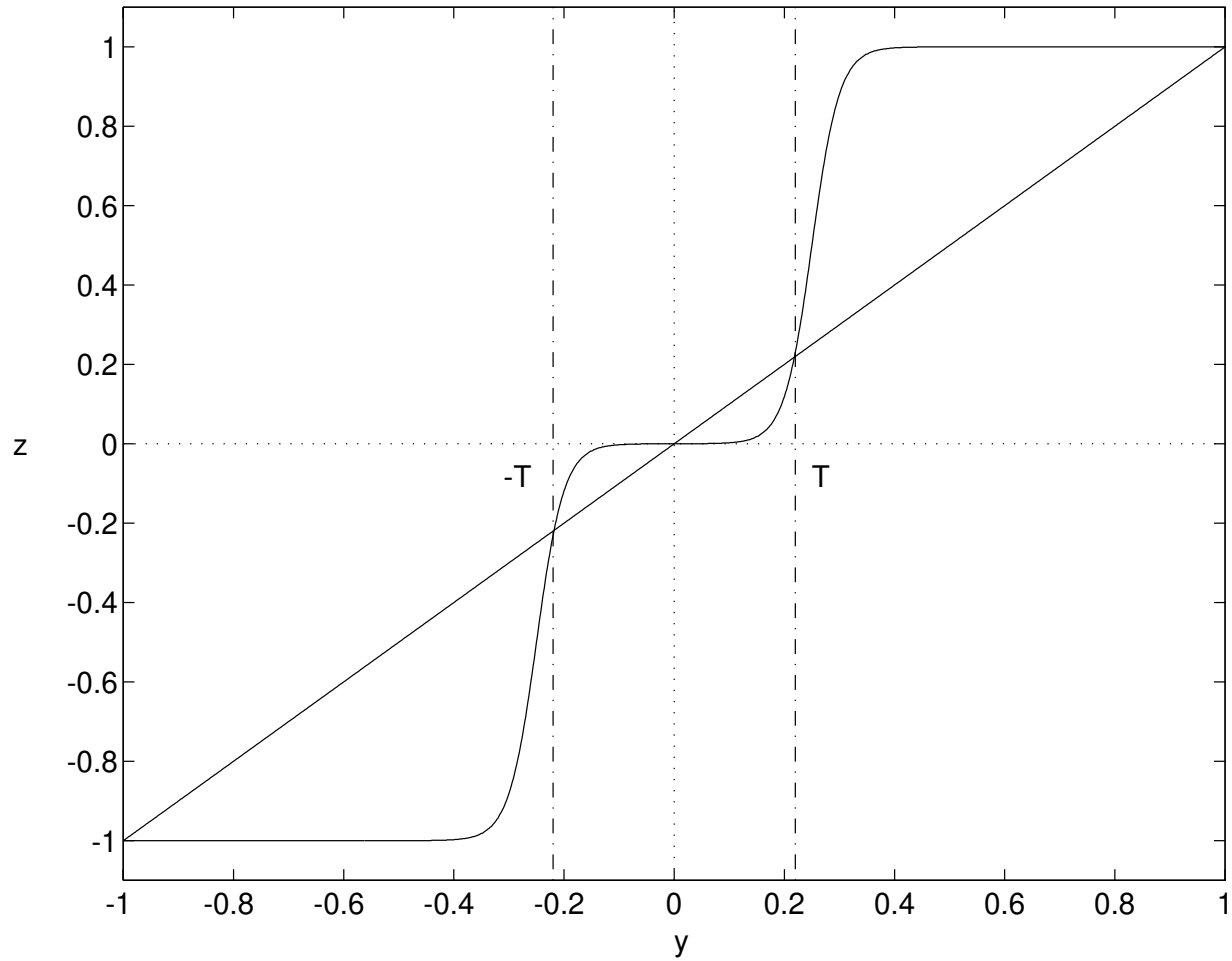
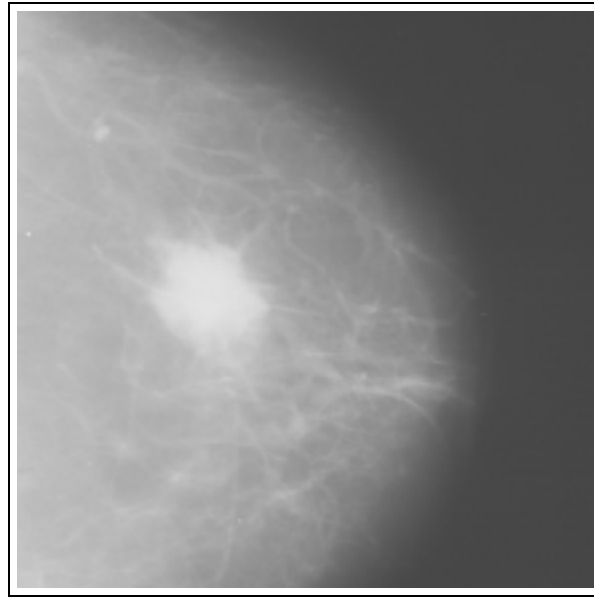
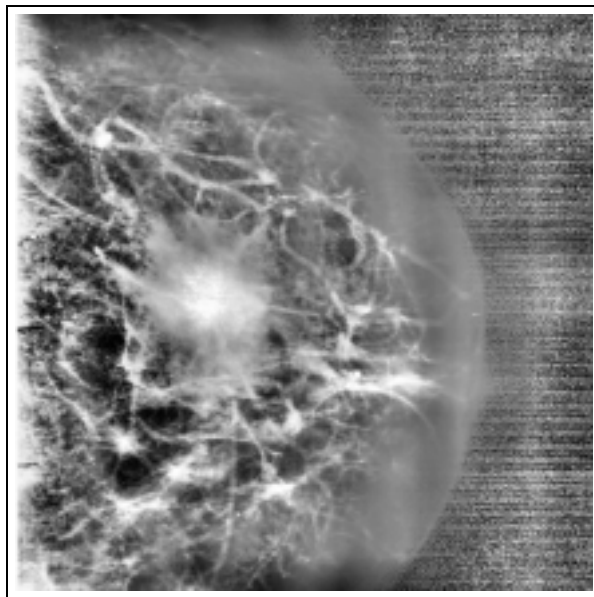


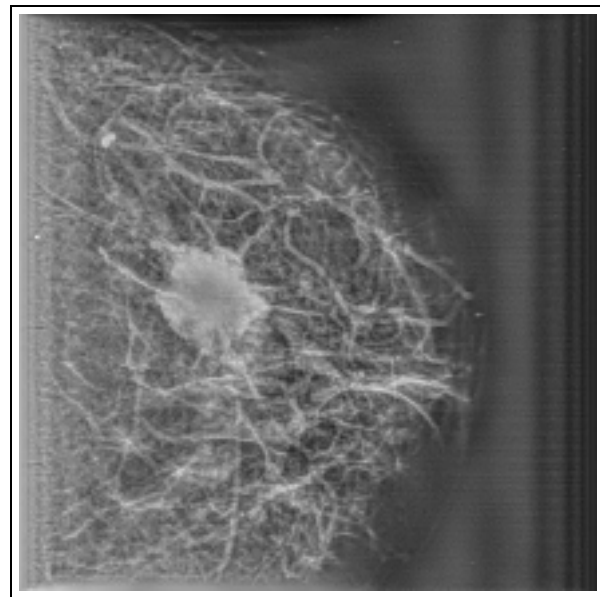
Fig. 11. Adaptive gain: $f(y)$ for $b = 0.25$ and $c = 40$ overlaid with $z = y$.



(a)



(b)



(c)

Fig. 12. (a) Mammogram with spicular mass, M73. (b) Enhancement by adaptive histogram equalization. (c) Global enhancement by multiscale adaptive gain processing of φ -transform coefficients.

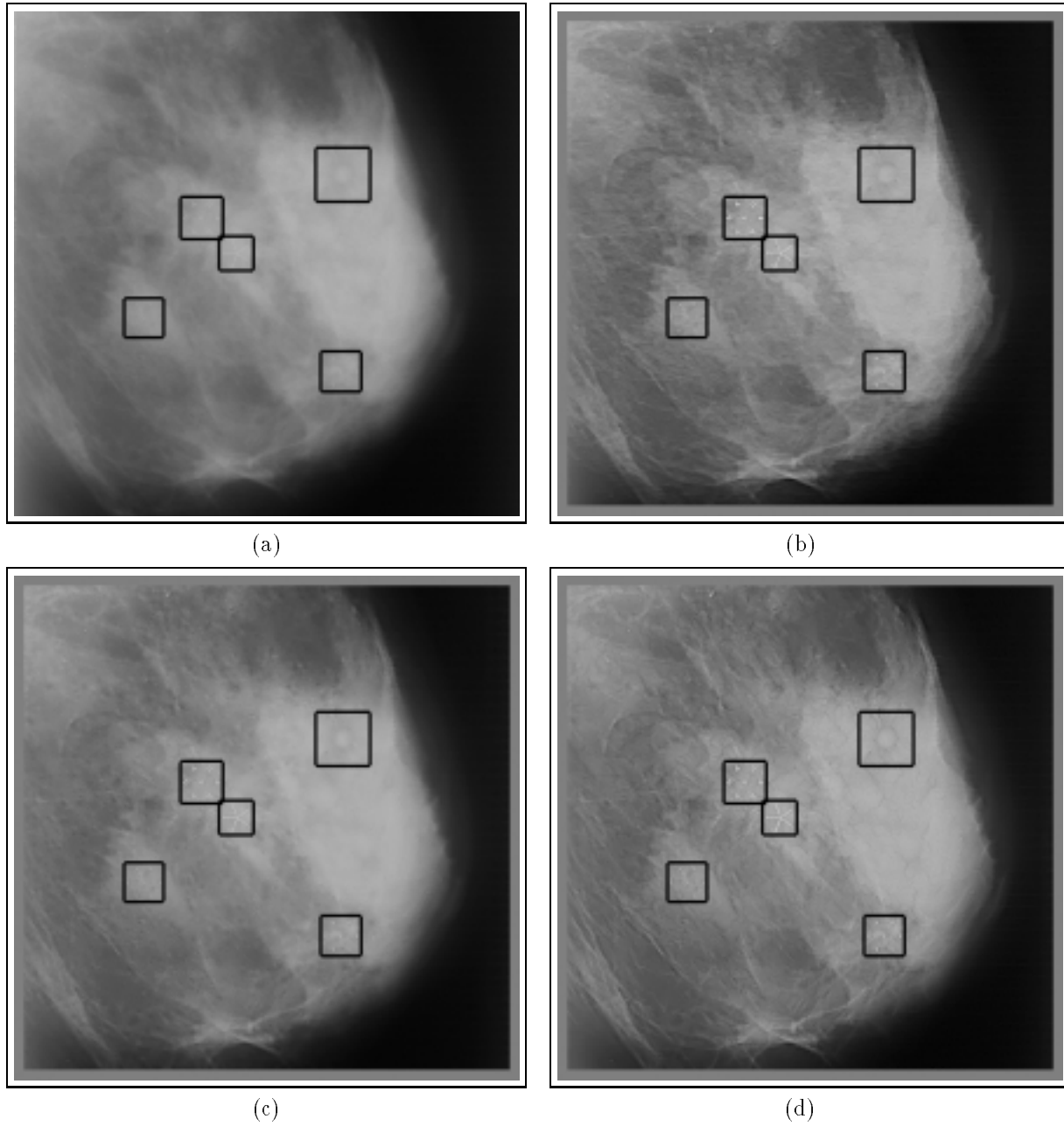


Fig. 13. Blended mammogram: (a) Enhancement by unsharp masking. (b), (c) and (d) Local enhancement by multiscale edges obtained from the dyadic wavelet transform, φ -transform, and hexagonal wavelet transform coefficients, respectively.

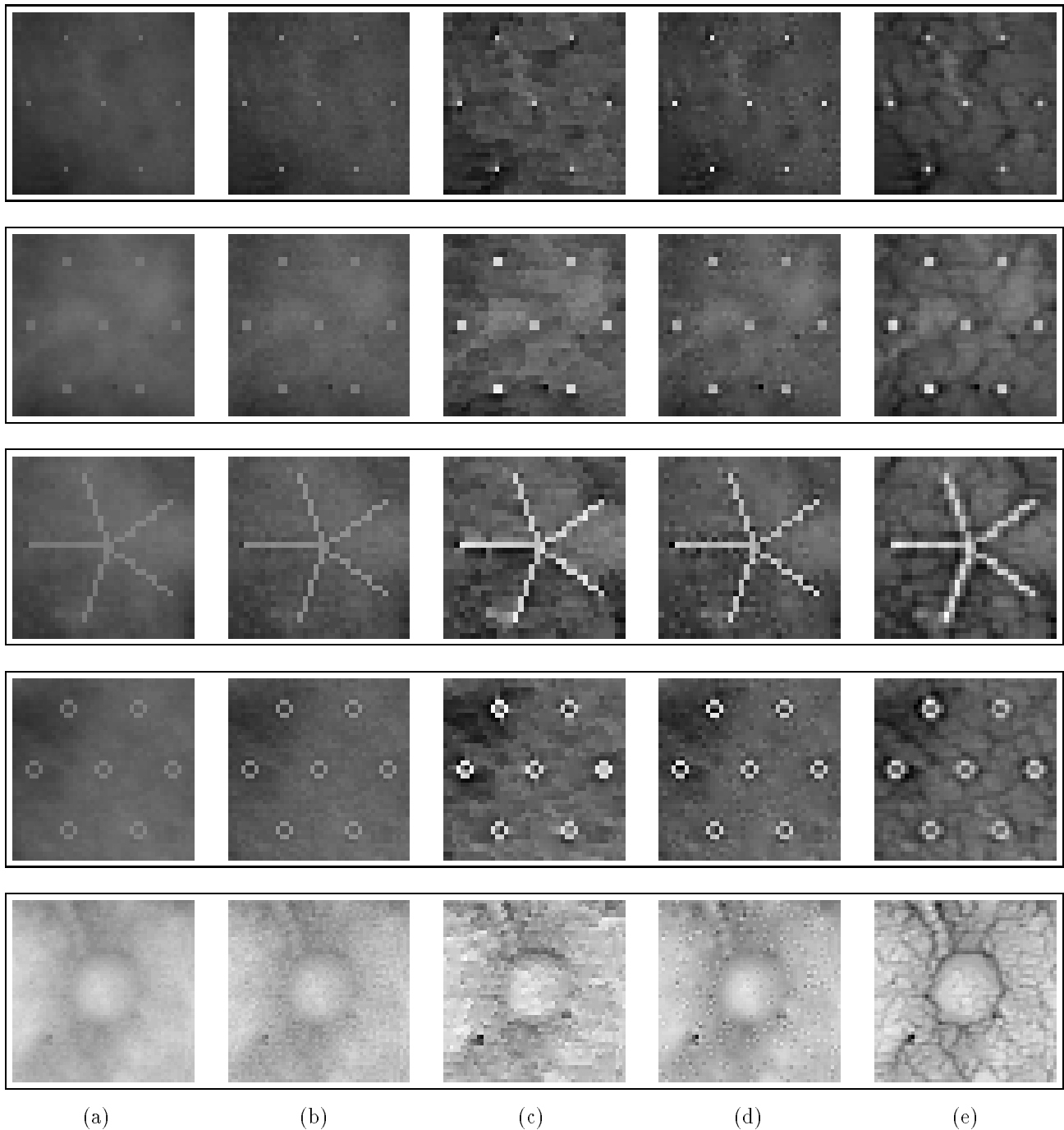


Fig. 14. Contrast enhancement for features in blended mammogram. Phantom mammographic features from top to bottom: minute microcalcification cluster, microcalcification cluster, spicular lesion, circular (arterial) calcification, and a well-circumscribed mass. (a) Original image. (b) Enhancement by unsharp masking. (c), (d) and (e) Local enhancement by multiscale edges obtained from the dyadic wavelet transform, φ -transform, and hexagonal wavelet transform coefficients, respectively.

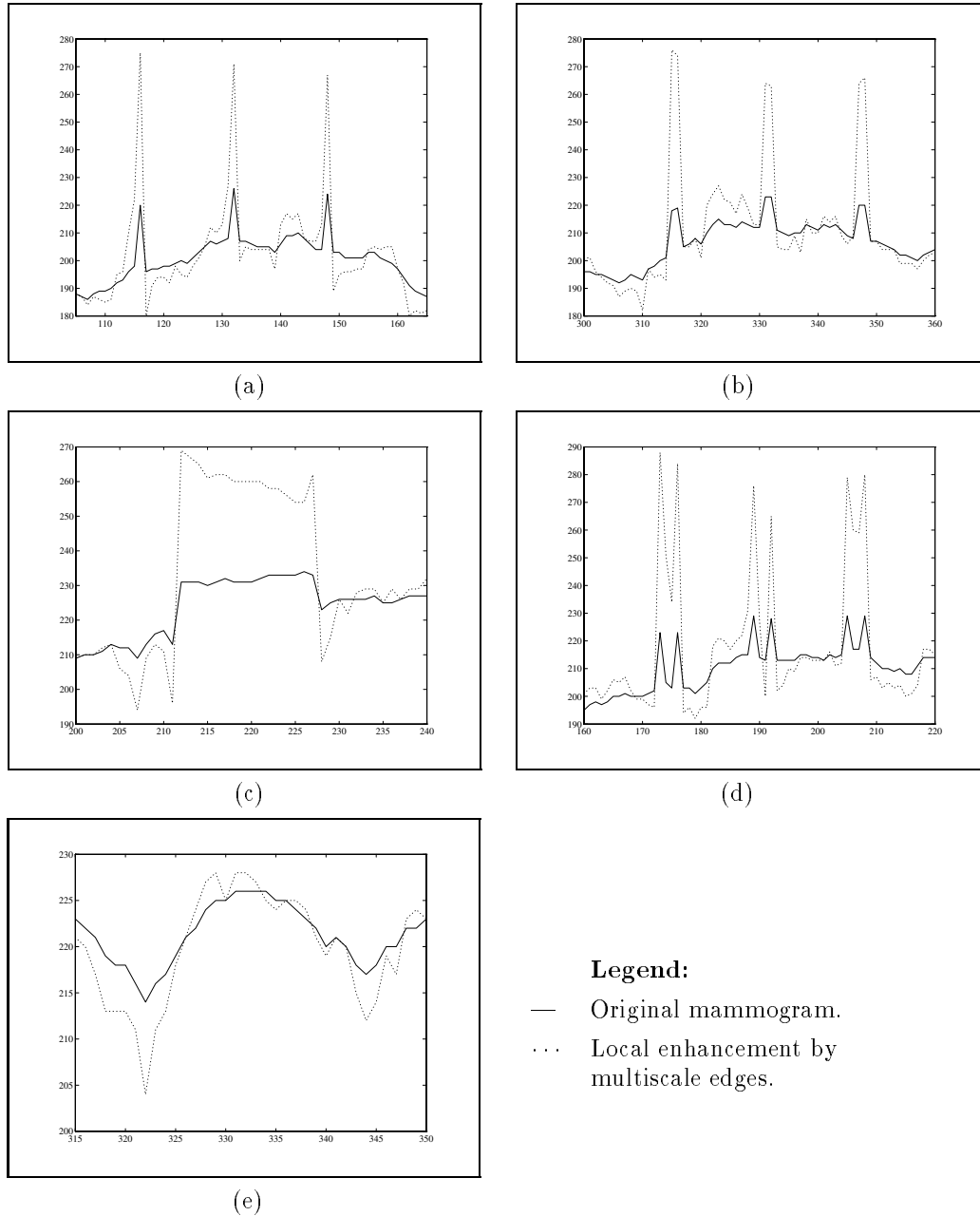


Fig. 15. Sample scan lines displaying local enhancement by the method of multiscale edges of a dyadic wavelet transform: (a) minute microcalcification cluster, (b) microcalcification cluster, (c) spicular lesion, (d) circular (arterial) calcification and (e) well-circumscribed mass.

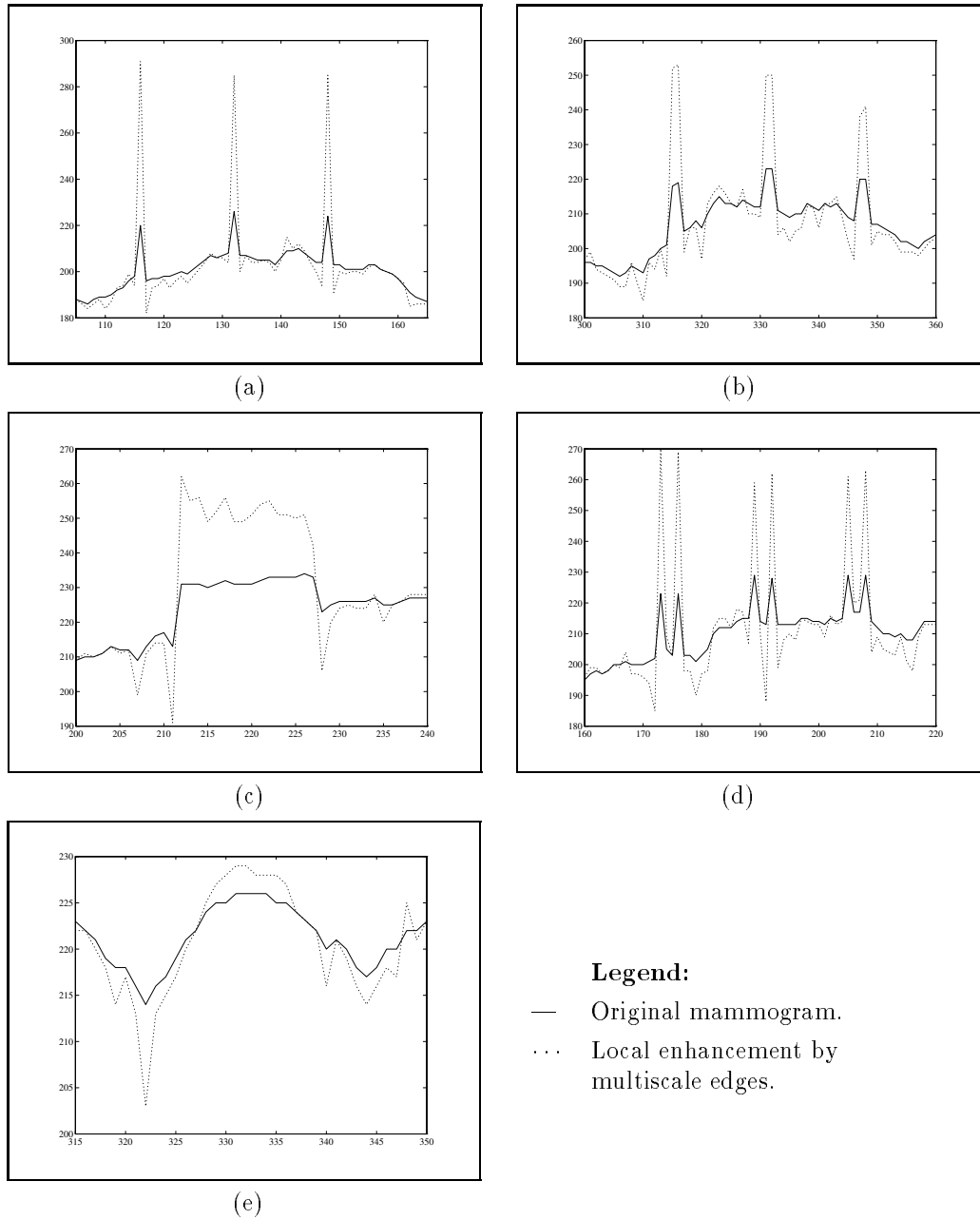


Fig. 16. Sample scan lines displaying local enhancement by the method of multiscale edges of a φ -transform: (a) minute microcalcification cluster, (b) microcalcification cluster, (c) spicular lesion, (d) circular (arterial) calcification and (e) well-circumscribed mass.

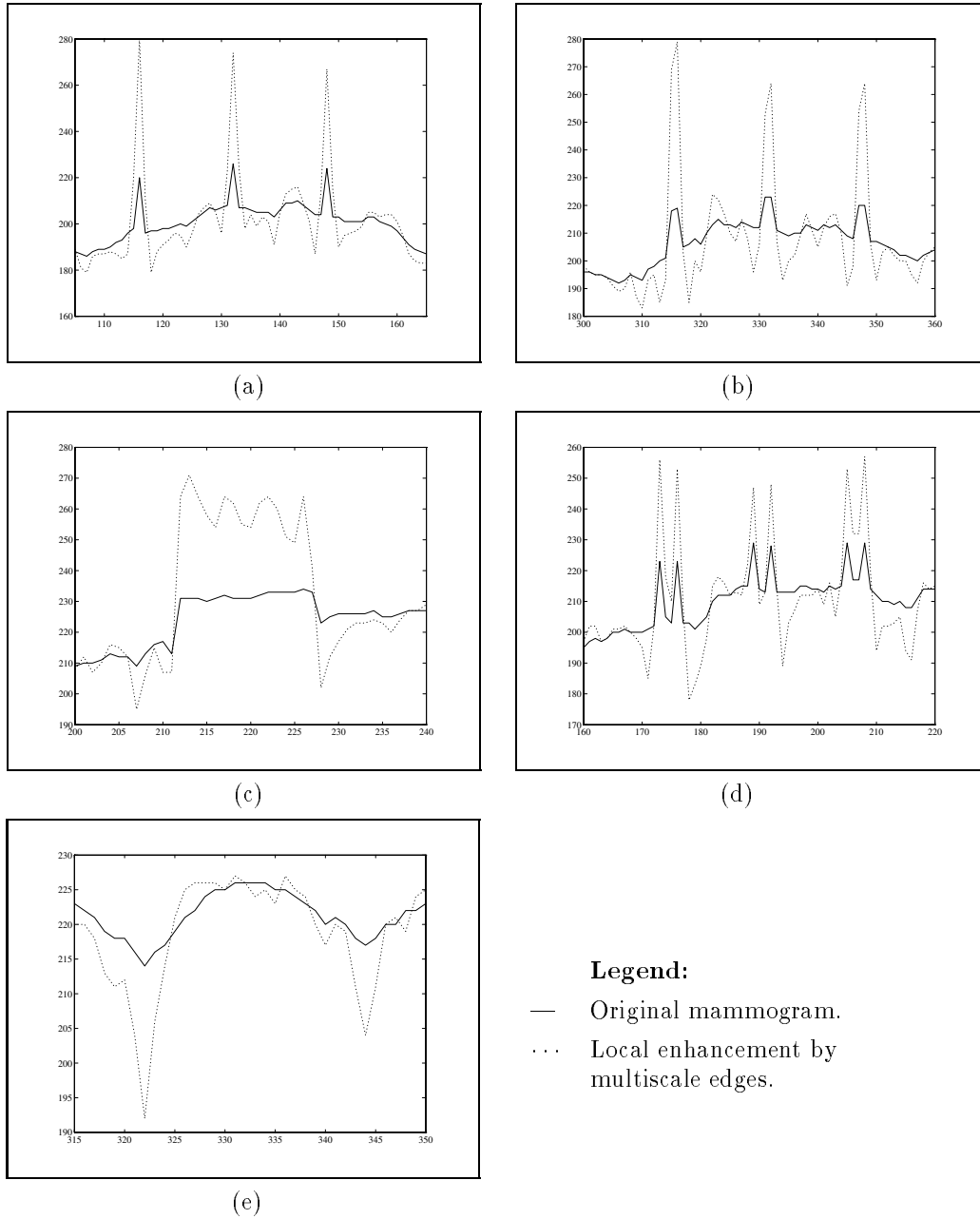


Fig. 17. Sample scan lines displaying local enhancement for the method of multiscale edges of a hexagonal wavelet transform: (a) minute microcalcification cluster, (b) microcalcification cluster, (c) spicular lesion, (d) circular (arterial) calcification and (e) well-circumscribed mass.

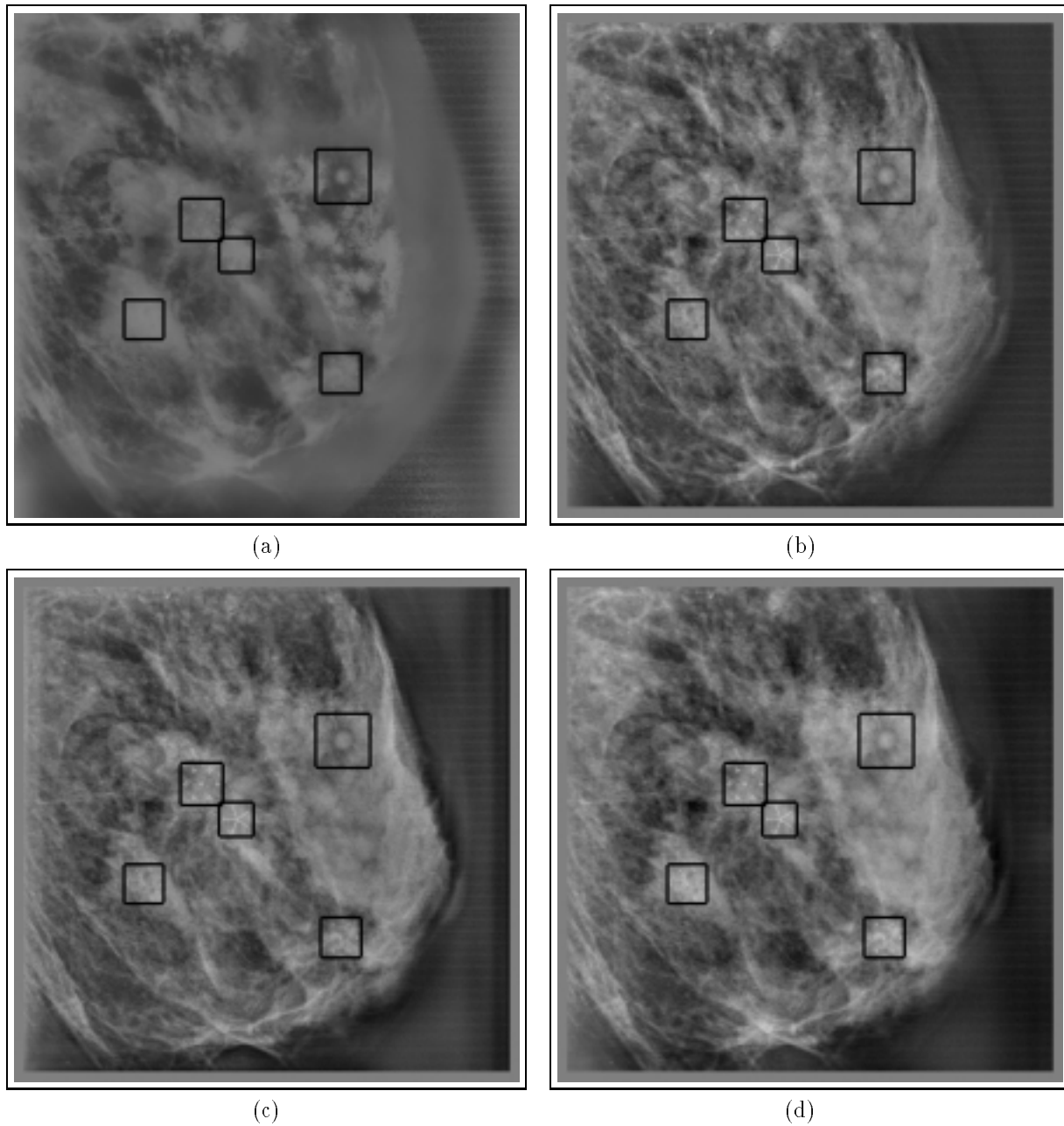


Fig. 18. Blended mammogram: (a) Enhancement by adaptive histogram equalization. (b), (c) and (d) Global enhancement by multiscale adaptive gain processing of the dyadic wavelet transform, φ -transform, and hexagonal wavelet transform coefficients, respectively.

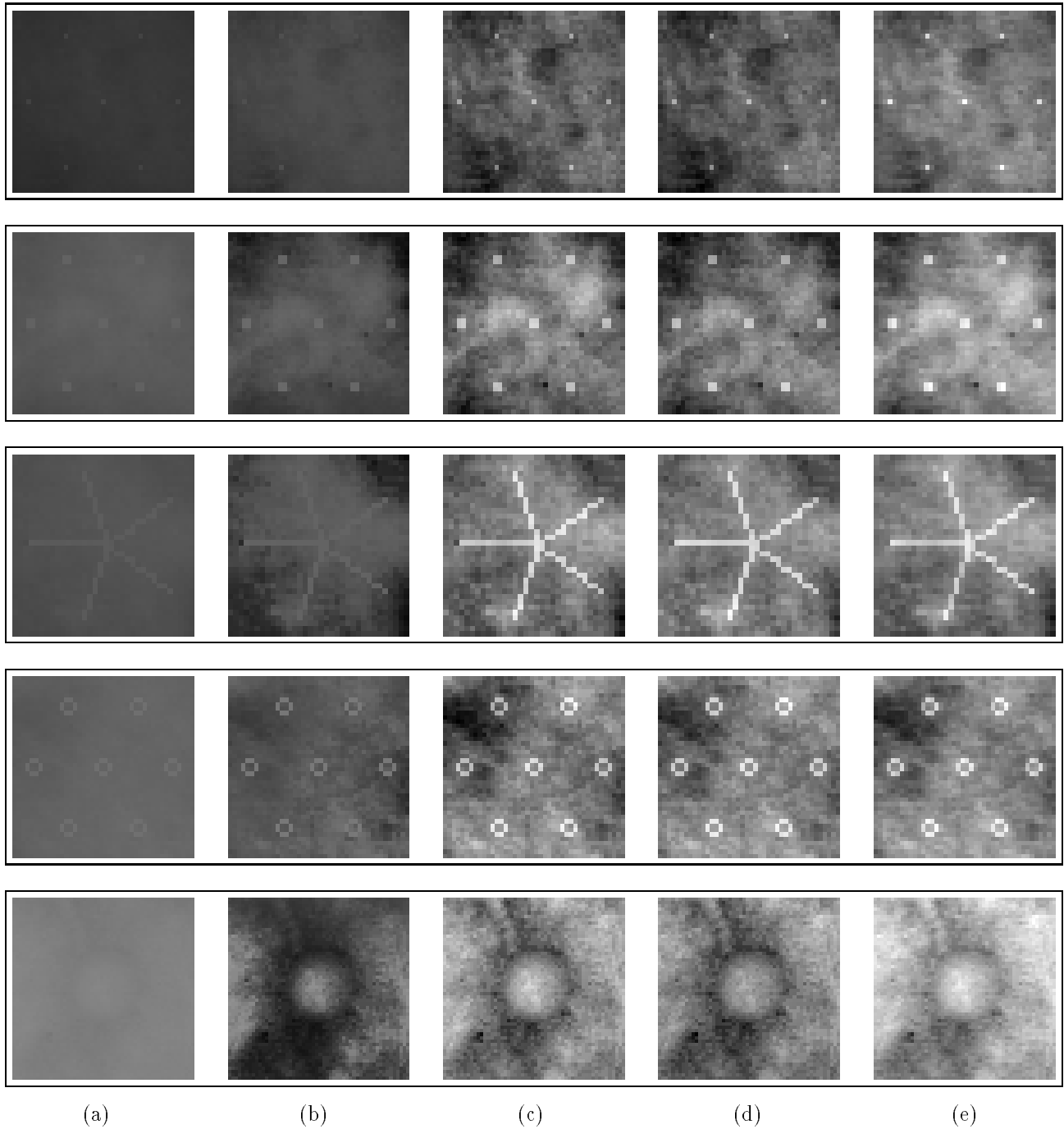


Fig. 19. Contrast enhancement for features in blended mammogram. Phantom mammographic features from top to bottom: minute microcalcification cluster, microcalcification cluster, spicular lesion, circular (arterial) calcification, and a well-circumscribed mass. (a) Original image. (b) Enhancement by adaptive histogram equalization. (c), (d) and (e) Global enhancement by multiscale adaptive gain processing of the dyadic wavelet transform, φ -transform, and hexagonal wavelet transform coefficients, respectively.